Author Contributions:

Conceptualization: David K. Ralston, W. Rockwell Geyer, Brian Dzwonkowski, David A. Honegger, Merrick C. Haller
Formal analysis: David K. Ralston, Christopher C. Wackerman, David A. Honegger, Merrick C. Haller
Funding acquisition: David K. Ralston, W. Rockwell Geyer, Brian Dzwonkowski, Merrick C. Haller
Investigation: David K. Ralston, W. Rockwell Geyer, Christopher C. Wackerman, Brian Dzwonkowski, David A. Honegger, Merrick C. Haller
Methodology: David K. Ralston, W. Rockwell Geyer, Christopher C. Wackerman, Brian Dzwonkowski, David A. Honegger, Merrick C. Haller
Project administration: Merrick C. Haller
Visualization: David K. Ralston

Interacting Influences of Diurnal Tides, Winds, and River Discharge on a Large Coastal Plume

David K. Ralston[1] , W. Rockwell Geyer[1] , Christopher C. Wackerman[2], Brian Dzwonkowski[3] , David A. Honegger[4] , and Merrick C. Haller[4]

[1]Woods Hole Oceanographic Institution, Woods Hole, MA, USA, [2]Naval Research Laboratory, Stennis Space Center, MS, USA, [3]Dauphin Island Sea Laboratory, Dauphin Island, AL, USA, [4]Oregon State University, Corvallis, OR, USA

Abstract The dispersal of large river plumes in the coastal ocean depends on multiple factors, and in some cases, can be categorized into distinct dynamical regimes: a tidally dominated near-field, a rotational mid-field, and a coastal current far-field. In this study, observations and modeling are used to evaluate the factors controlling the variability in the buoyant plume from Mobile Bay. Rather than distinct dynamical regimes, the Mobile Bay plume depends on forcings that act at overlapping temporal and spatial scales: diurnal tides, river discharge events, and winds. Satellite synthetic aperture radar images along with shipboard in-situ sampling and marine radar are used to observe plume fronts in spring 2021. Hydrodynamic model simulations are compared with observations and used to characterize a large coastal plume at consistent tidal phase across a range of forcing conditions. The along-shore position of the plume depends primarily on advection by wind-driven surface currents. The cross-shore extent and plume area depend primarily on the tidal amplitude and river discharge, and secondarily on northerly (seaward) winds. Along-shore winds influence the buoyancy anomaly by altering salinity in the estuary and offshore. Upwelling winds increase the buoyancy anomaly and advect previous plumes away from the mouth. Downwelling winds reduce the buoyancy anomaly by trapping previous plumes near the coast and directing freshwater discharge toward a secondary outlet. Thus, the combined, overlapping influences of the tide, wind, and discharge dominate the variability in freshwater delivery to the shelf at time scales of days and distances of tens of km.

Plain Language Summary Buoyant river plumes discharge into the coastal ocean and alter the distribution of freshwater and material like sediment and nutrients. This study examines the factors affecting the plume from Mobile Bay in the Gulf of Mexico. The research integrates shipboard measurements, satellite imagery, and numerical modeling to capture the variability in the plume in spring 2021. Plumes are often characterized with distinct regions where particular physical processes dominate—the tide or river discharge close to the mouth, and the earth's rotation and wind as the plume spreads and transitions into a coastal current. However, for Mobile Bay the winds, tides, and river discharge all contribute significantly to the size and position of the plume. Along-shore winds drive coastal currents that transport the plume, upwelling or downwelling winds move the plume offshore or trap it near the coast, and shallow stratification increases the direct influence of the wind. Diurnal tides drive outflows that are much larger than the scale of influence of the earth's rotation, and river discharge varies substantially with meteorological events. The influences of the wind, tides and discharge cannot be cleanly separated in determining the fate of outflow from Mobile Bay and similar systems.

1. Introduction

River outflows enter the ocean as buoyant plumes and transform the physical and biogeochemical conditions of the coastal zone (Milliman & Farnsworth, 2013). The discharge of relatively fresh water alters the ambient stratification and can create buoyant coastal currents that affects circulation on the shelf (Lentz, 2004; Morey et al., 2003). The transformation of a plume as it interacts and mixes with coastal water depends on geo-morphologic factors and on forcing variables like the tides, wind, river discharge, the Earth's rotation, and the ambient water properties (Horner-Devine et al., 2015 and references therein).

Plumes are often characterized as having distinct dynamical regions as they expand away from a river mouth (Garvine, 1984; Hetland, 2005; Horner-Devine et al., 2009). For example, Horner-Devine et al. (2009) characterize river outflows as having three distinct dynamical regimes. In the near-field plume, inertia from the estuarine outflow due to the tide or river discharge dominates the spreading relative to the buoyancy or winds. In the mid-

Writing – original draft: David
K. Ralston
Writing – review & editing:
W. Rockwell Geyer, Christopher
C. Wackerman, Brian Dzwonkowski,
David A. Honegger, Merrick C. Haller

field, the Earth's rotation turns the plume toward the coast, with additional influences from the ambient currents and the wind. In the far-field, the plume transitions into a coastal current that depends primarily on Coriolis, wind, and the cross-shore density gradient. The time scales increase with the spatial scales, from near-field advection of hours to the mid-field with recirculation for several days to the far-field that varies more slowly.

The trajectory of a plume through these dynamical regimes depends on conditions that vary at tidal, event, and seasonal time scales. The plume spreads as a gravity current due to the buoyancy anomaly between the estuarine outflow and the ambient offshore (Hetland & MacDonald, 2008; Wright & Coleman, 1971), and each water mass can vary with the tidal amplitude, river discharge, and wind. The surface density front between the plume and ambient waters can have horizontal spatial scales of a few meters and is a region of intense mixing and down-welling (Garvine, 1974). Turbulence at the plume front and the pycnocline below mix the outflow with ambient, reducing the buoyancy anomaly and changing the gravity current speed (Jurisa et al., 2016). Ambient currents driven by the tides, surface wind stress, or larger scale coastal circulation can also alter the propagation of the plume front.

Forcing conditions can alter plume and ambient conditions at time scales that overlap with the transitions through the dynamical regions, compromising the applicability of conceptual models. Here we examine how a large river plume depends on the wind, tidal, and river forcing. The focus is the outflow of Mobile Bay into the Gulf of Mexico. Important aspects affecting the plume size and structure include diurnal tides, large and variable river inputs, a shallow ebb delta at the mouth of the bay, stratified conditions on the shelf, and frequent passage of weather systems. Characterizing the large scales of river plumes (tens of km) with synoptic, shipboard sampling is challenging. Here we combine remote sensing, in-situ measurements, and hydrodynamic modeling to diagnose how tides, wind, and river discharge contribute to the observed variability. We show how the large spatial scales and overlapping temporal scales of the wind and tide blur the distinction between the near-field and mid-field dynamical regions and limit the influence of rotation on plume structure. The heterogenous response of the Mobile Bay outflow to these factors is distinct from some other large plumes (e.g., Garvine, 1984; Horner-Devine et al., 2009) and provides useful context for systems with similar forcing conditions.

2. Methods

2.1. Study Site

Mobile Bay is a large estuary on the U.S. Gulf Coast with an embayment 50 km long and 15–35 km wide (Figure 1). Freshwater input is primarily from the Alabama and Tombigbee Rivers, which merge to form the tidal Mobile River at the northern end of the bay (Dykstra & Dzwonkowski, 2020). The coastal discharge is the fourth largest in the contiguous U.S., with a mean of 1,900 m^3/s and a seasonal range from around 100 m^3/s during summer and early fall to more than 15,000 m^3/s during major events. The tide is microtidal and primarily diurnal (Figure 2). Fortnightly variation in tidal amplitude is primarily influenced by the declination of the moon, with tropic tides (or diurnal spring tides) when the declination angle is the highest having the greatest tidal range (0.8–0.9 m) and equatorial tides (or neaps) when the declination angle is the lowest having ranges of 0.1–0.2 m (Dinnel et al., 1990; Seim et al., 1987).

The primary connection between Mobile Bay and the shelf is through Main Pass between Dauphin Island to the west and Morgan Peninsula to the east (Figure 1). Main Pass is about 5.5 km wide, with a dredged navigation channel of 15 m and broad shoals on either side. Sand Island Shoals, located on the west side of the ebb delta, are 3–4 m deep while Dixey Bar, bordering the navigation channel to the east, is shallower. Tidal velocities in Main Pass reach 1.7 m/s during tropic tides and are much weaker (0.1–0.3 m/s) during equatorial tides (Dinnel et al., 1990). A second, shallow (<3 m) outlet connects the bay to Mississippi Sound via Pas-aux-Herons between Dauphin Island and the mainland. On average, Main Pass accounts for about 2/3 of the tidal exchange (Kim & Park, 2012).

The salinity and stratification in Mobile Bay depend primarily on the river discharge, although wind also plays a role (Coogan & Dzwonkowski, 2018; Noble et al., 1996; Schroeder et al., 1990). During low discharge the salinity intrusion extends to the northern end of the bay, whereas during high discharge the near-surface outflow at the mouth can be nearly fresh (Coogan & Dzwonkowski, 2018; Dzwonkowski et al., 2015). River discharge gauges are located at the landward limit of a tidal river network that extends 150 km upstream from the bay. The lag
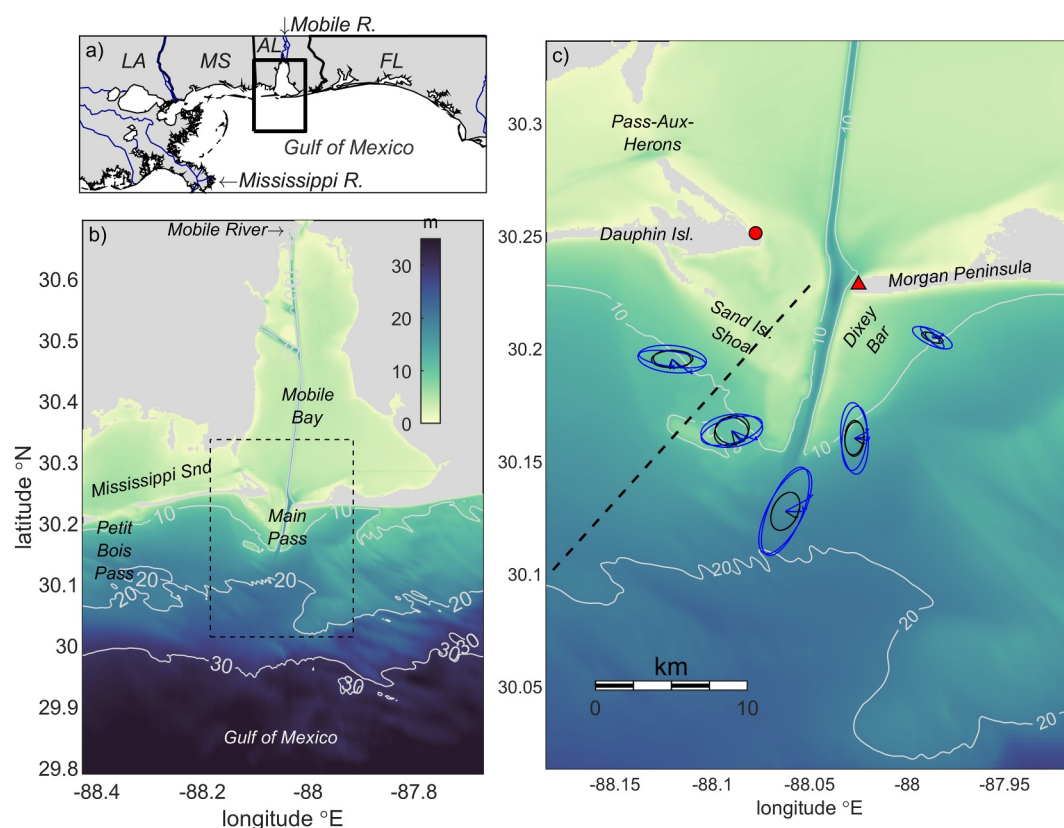
Figure 1. Model bathymetry. (a) Regional map, with box marking the model grid; (b) model grid; (c) zoom on mouth region, marking the location of the transect shown in Figure 3 with a dashed black line. Tidal ellipses from model results at locations near the 10 m isobath are shown for the main diurnal tidal constituents (K1 and O1) for the surface (blue) and depth-averaged (black) currents. Monitoring stations at Dauphin Island (red circle, salinity and water level) and Fort Morgan (red triangle, wind) are marked.

between observed water level at the gauges and water level at the head of the bay is 3–5 days, and the lag for water level at the mouth is 4–9 days (Dinnel et al., 1990; Dykstra & Dzwonkowski, 2020; Dzwonkowski et al., 2015).

The shelf outside Mobile Bay is wide and shallow, and wind-driven currents play a prominent role. The synoptic variability includes Ekman response and cross-shelf transport enhanced by stratification (Dzwonkowski & Park, 2012; Dzwonkowski et al., 2014; Dzwonkowski, Park, & Jiang, 2011). During the spring and early summer, wind comes increasingly from the southeast with the strengthening of the Bermuda high, but cold fronts bring episodic shifts and winds from the southwest and northwest (Schroeder & Wiseman, 1985). Along-shelf currents are highly coherent with the wind, resulting in subtidal water level variability at the mouth of the bay and upwelling or downwelling on the shelf (Dzwonkowski & Park, 2012; Dzwonkowski et al., 2015). Cross-shelf winds have less coherence with currents on the shelf due to the influence of the estuarine outflow, but cross-shelf (along-estuary) winds can influence water levels in the bay (Dzwonkowski & Park, 2012; Kim & Park, 2012; Noble et al., 1996). Subtidal flows on the shelf are relatively weak (few cm/s) and generally to the east during the higher discharge in spring and summer and reverse to the west during the fall due to the seasonal wind forcing (Dzwonkowski & Park, 2012). River discharge influences salinity on the shelf along with wind-driven upwelling or downwelling at synoptic time scales (Dzwonkowski, Park, Kyung Ha, et al., 2011).

Plumes from Mobile Bay have been observed in satellite imagery using multiple platforms, but close examination of their structure and extent has been limited (Dzwonkowski, Park, Kyung Ha, et al., 2011). Plume size in Landsat imagery over 11 years was primarily linked to river discharge but also depended on tidal phase and amplitude (Dinnel et al., 1990). Based on spectral reflectance measurements (indicative of suspended sediment) during a week of high discharge and diurnal spring tides, plume size correlated with tidal prism and plumes responded rapidly to along-shore winds (Stumpf et al., 1993). Ocean color observations during a high discharge period
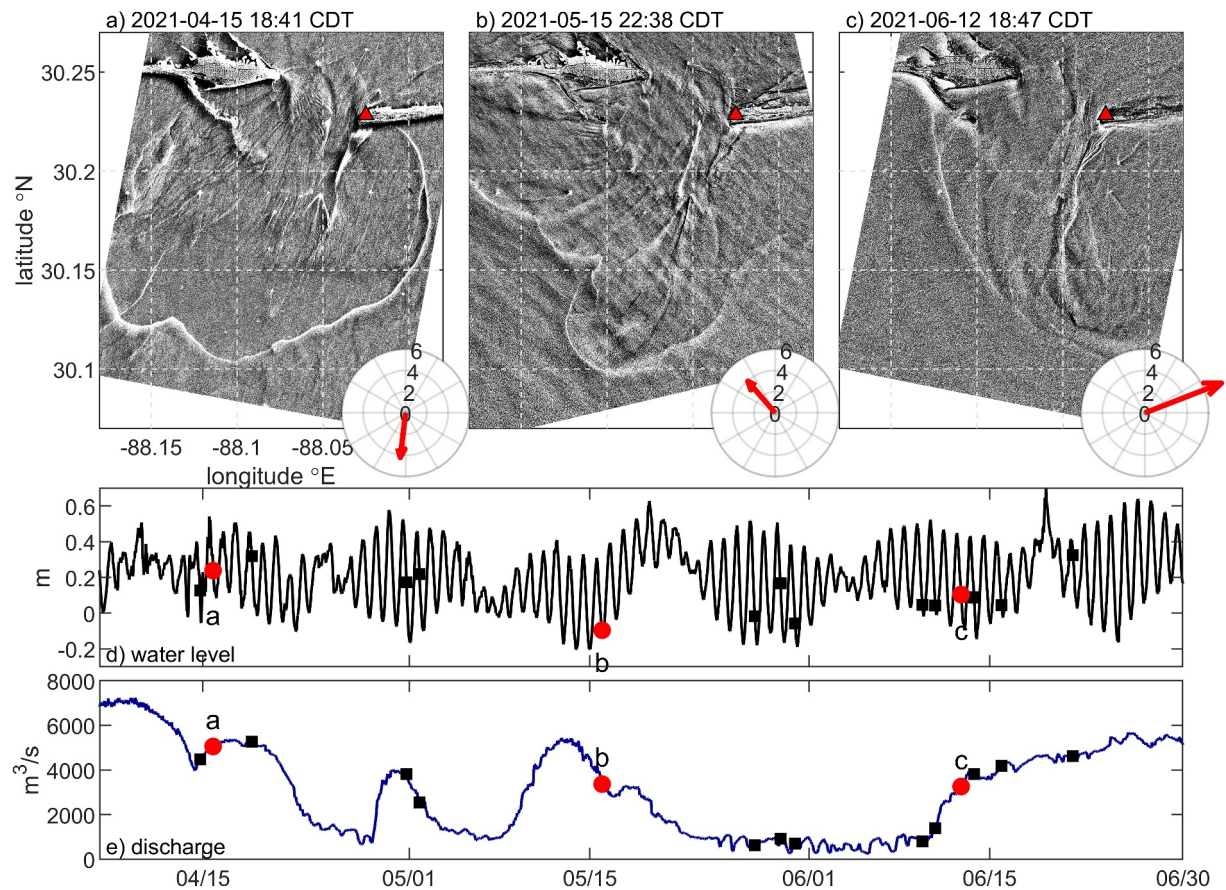
Figure 2. Example plumes with forcing conditions. Synthetic aperture radar (SAR) images for plumes in (a) April, (b) May, and (c) June with wind speed (m/s) and direction for each as inset; (d) water level time series from Dauphin Island; (e) discharge for the Mobile River based on observed discharge at USGS gauges lagged by 4 days and multiplied by 1.07 to account for transit time and downstream inputs. Times of SAR images shown here are marked in (d) and (e) with red dots; times of other SAR images with visible plume fronts are marked with black squares (see Supporting Information S1). Red triangles in SAR images show the location of wind observations at Fort Morgan.

revealed that plumes responded to the along-shore wind, elongating with downwelling and widening with up-welling (Dzwonkowski et al., 2015). The main tidal plume is typically about 2 m thick, and remnants of previous plumes can persist as stratified layers on the shelf and as surface fronts near the mouth (Dzwonkowski et al., 2015).

2.2. Observations

Observations were collected near the mouth of Mobile Bay during June 2021 as part of the Under Sea Remote Sensing project sponsored by the Office of Naval Research. Shipboard surveys were conducted from the *R/V Pelican* 9–15 June 2021. Transect measurements were made with a fast-profiling conductivity-temperature-depth (CTD) sensor deployed from a winch and sampling at 16 Hz. Horizontal spacing between CTD profiles was typically 40–50 m, and data were interpolated onto regular profiles with a vertical spacing of 10 cm. Additionally, a submerged tow-body with upward- and downward-looking acoustic Doppler profilers (Nortek Signatures) was towed behind the ship using a depressor wing. Shipboard surveys focused on sampling the plume front at locations around the mouth during ebb tides. Transect data shown here was collected on 12 June on the west side of the mouth (see Figure 1 for location), with repeated passes shifting seaward with the propagating plume front.

As part of the same observational campaign, X-band marine radar data were collected from the *R/V Point Sur* during 9–15 June 2021. The marine radar system transmitted and received radiation at 9.65 GHz with pulses of length 90 ns that were repeated at 2 kHz. The 3 m long, horizontally-polarized antenna rotated at 48 RPM, and location and heading were determined using a shipboard GPS and compass. With these settings, the polar-

coordinate pixel resolution was 12 m in range (oversampled to 3 m) and 1 deg in azimuth (oversampled to 0.5 deg). Fronts and other backscatter signatures associated with sharp surface current gradients were isolated from the dominant surface gravity wave signatures by pixelwise averaging 2 min of rotations (roughly 100). Radar image data were collected in the vicinity of the *R/V Pelican* during its transects of the western plume front on 12 June.

Satellite synthetic aperture radar (SAR) imagery focused on the mouth of Mobile Bay was collected from April to June 2021. SAR images were downsampled in the ground plane by averaging the original higher resolution data to 10-m spacing. Downsampled images were median-flattened with a 100×100 pixel median filter. This allows estimation of noise-reduced radar cross section modulations across features with spatial scales of plume fronts while removing modulations from larger scale phenomena. Finally, the median filtered images were remapped into a regular latitude/longitude grid with pixel resolution of about 15 m. SAR intensity (amplitude squared) is normalized by mean image intensity in a fixed region in the ocean offshore and then linearly mapped into the range [0,255] for plotting. A total of 59 SAR images were collected and 15 of those had ebb plume fronts visible as bright, curved features.

The brightness in the SAR imagery is directly proportional to the amplitude of small waves (on the order of 5-cm wavelengths) that are resonant with the SAR radiation. Thus, changes in brightness are caused by processes that influence these wave amplitudes: mainly surface currents, winds, and larger-scale waves (Wackerman, 2023). Over spatial scales where winds can be considered constant, convergence or divergence in surface currents dominate the changes in the small wave amplitudes and thus the SAR image modulation. To a lesser extent, the larger-scale wavefield also affects the small-scale waves by tilting the water surface and inducing additional surface velocities, altering the resonant wavelength and the amplitude of the scattering. The interaction of larger scale waves with the Bragg-scale facets can be modeled by assuming conservation of wave action to calculate changes in the wave spectra due to currents and accounting for tilted scattering (Wackerman, 2023).

Time series monitoring data from various sources are used for model forcing and evaluation. Discharge data were collected from the USGS stations for the Alabama (at Clairborne, #02428400) and Tombigbee (at Coffeeville, 02469761) Rivers. These rivers converge to form the tidal Mobile River. Water level monitoring by NOAA was collected at stations around Mobile Bay including Dauphin Island (8735180) near the mouth and Coast Guard Sector Mobile (8736897) in the upper bay. Wind data were collected from the NOAA station at Fort Morgan (8734673) near the mouth. Water level and near-surface salinity measurements were also collected from the Alabama Real-Time Coastal Observing System (ARCOS) operated by the Dauphin Island Sea Lab (DISL). During the period of observations, the Dauphin Island and Bon Secour stations were operational.

2.3. Model

An application of the Regional Ocean Modeling System (ROMS) (Haidvogel et al., 2008; Shchepetkin & McWilliams, 2005) was developed to simulate circulation, salinity, and temperature in Mobile Bay and the adjacent shelf. The horizontal grid (600 by 700 grid cells) extends from the head of the bay to 50 km onto the shelf and about 40 km east and west of the mouth (Figure 1). The horizontal grid resolution is maximum near the mouth at 70–80 m and grid spacing increases into the bay (100–150 m along-estuary) and offshore (increasing to 250 along-shore and 400 m cross-shore near the boundaries). Bathymetry was constructed using data from the 1/9th arc-second Continuously Updated Digital Elevation Model from the National Centers for Environmental Information. Additional bathymetric data were incorporated from a survey conducted in April 2021 of the ebb-tide delta (S. Harrison, pers. comm.), a region that has highly dynamic morphology (Morton, 2008). The vertical grid has 25 sigma levels with closer spacing near the surface. The model includes temperature as a state variable, but salinity dominates the buoyancy signal of the plume during the study period. For example, using the depth averaged temperature rather than surface and bottom values alters the stratification at the mouth by about 5%.

Simulations with realistic forcing were run for April through June 2021. Observed discharge from the Alabama and Tombigbee Rivers was increased by a factor of 1.07 to account for inputs between the USGS stations and the model domain and was lagged by 4 days to account for transit time through the tidal river (Dykstra & Dzwonkowski, 2020; Schroeder, 1978). The observed lag can depend on discharge (Dykstra & Dzwonkowski, 2020) but that was not incorporated here. Spatially and temporally varying atmospheric forcing was derived from NOAA North American Mesoscale model analyses output with 12-km grid resolution, but wind speeds were increased by 20% based on a comparison with observed wind speeds at Fort Morgan. Tidal forcing was based on the ADCIRC

database (version ec2001_v2e). Salinity, temperature, and subtidal water level at the open boundaries were derived from archived model output of the NOAA Northeast Gulf of Mexico Operational Forecast System (NEGOFS).

Initial model development included calibration to prior observations. Time series of water level, temperature, and salinity from the ARCOS and NOAA monitoring stations were compared with model simulations for the spring of 2019. Additionally, salinity and temperature profiles from the model were compared with CTD profiles from surveys in Mobile Bay from April 2019 (Coogan et al., 2021). Adjustment of the bottom roughness was the primary means of calibration, and a uniform, constant $z_0 = 2$ cm compared well with the observations. Subsequent comparisons of the model results with observations including time series, shipboard surveys, and SAR imagery from the spring of 2021 are described in the Results and Supporting Information S1.

In addition to the simulations with realistic forcing, diagnostic cases were run with idealized wind forcing. Wind was prescribed to be uniform and constant at a moderate speed of 4 m/s for cases representing the dominant wind directions during the study period: from the southwest, from the southeast, and from the north. The idealized wind cases were run for the early June 2021 period of shipboard observations. All the other forcing conditions (river discharge, boundary conditions) and model parameters in the idealized cases remained the same as for the realistic simulation except for the wind.

3. Results

3.1. Plume Observations and Modeling

Representative examples of SAR images of plume fronts are shown along with the tidal water level and river discharge (Figure 2). On April 15, a large and symmetric plume was observed following a period of high river discharge ($\sim$5,000 m^3 s^{-1}) with moderate tides and northerly wind (Figure 2a). On May 15, river discharge was similar ($\sim$4,000 m^3/s) but the wind was from the southeast and the plume front was shifted to the west as several distinct frontal arcs (Figure 2b). This contrasts with the SAR image from June 12 when discharge was also around 4,000 m^3/s but the wind was from the southwest causing the plume to be shifted to the east. Additional examples of plume fronts in SAR images are in Supporting Information S1. Most of the SAR imagery that had distinct plume fronts occurred during the stronger tropic tides. This likely reflects stronger surface convergence at the fronts due to fresher outflow and stronger ambient currents. Some SAR images during weaker equatorial tides had front-like features scattered throughout the coastal ocean but they were less clearly associated with plumes from Mobile Bay.

The SAR imagery is rich in structure associated with spatial variability in the currents. The plume fronts are sharp, bright features that have increased radar cross-section due to increased surface roughness from convergence between the buoyant plume and the ambient water. The spatial extent and locations of plume fronts differ day-to-day, but other features are more consistent between SAR images (Figure 2). Bright regions of stronger scattering mark the edges of the navigation channel south of Fort Morgan, with the eastern edge of the channel brighter on some days (Figures 2a and 2c) and the western edge on others (Figure 2b). Bathymetric features like the Sand Island shoals and the shallow Main Pass east of Dauphin Island also are regions of brighter backscatter. Flow through the gaps in the shoals correspond to streaks of alternating brighter and darker regions that in many cases connect to the plume fronts.

To assess how features in the SAR imagery correspond with water column properties we focus on the image from June 12 that had contemporaneous in-situ observations (Figure 3). Shipboard surveys transected the plume front as it propagated offshore and documented the structure of the plume and the ambient. The waters offshore were continuously stratified from the surface to 8 m depth with a salinity difference of about 3 psu (Figure 3c). In the SAR image, the surface plume front is a bright line of increased radar cross-section to the west of the mouth. The plume front is also clearly visible in the shipboard radar aboard the *R/V Point Sur* at the same time (labeled F1 in Figure 3e). An additional, weaker front appears in the marine radar image as an arced region of increased backscatter closer to the ship (labeled F2 in Figure 3e). The plume front in the shipboard surveys corresponded with a surface salinity gradient moving offshore (at $-3,400$ m in Figure 3c) and was a convergence zone with foam and other buoyant material. An additional surface convergence zone of buoyant material was observed visually from the ship seaward of the plume front and was associated with a subsurface bore (at $-3,900$ m in Figure 3c). The subsurface bore also appeared as increased brightness in the marine radar image at times when the
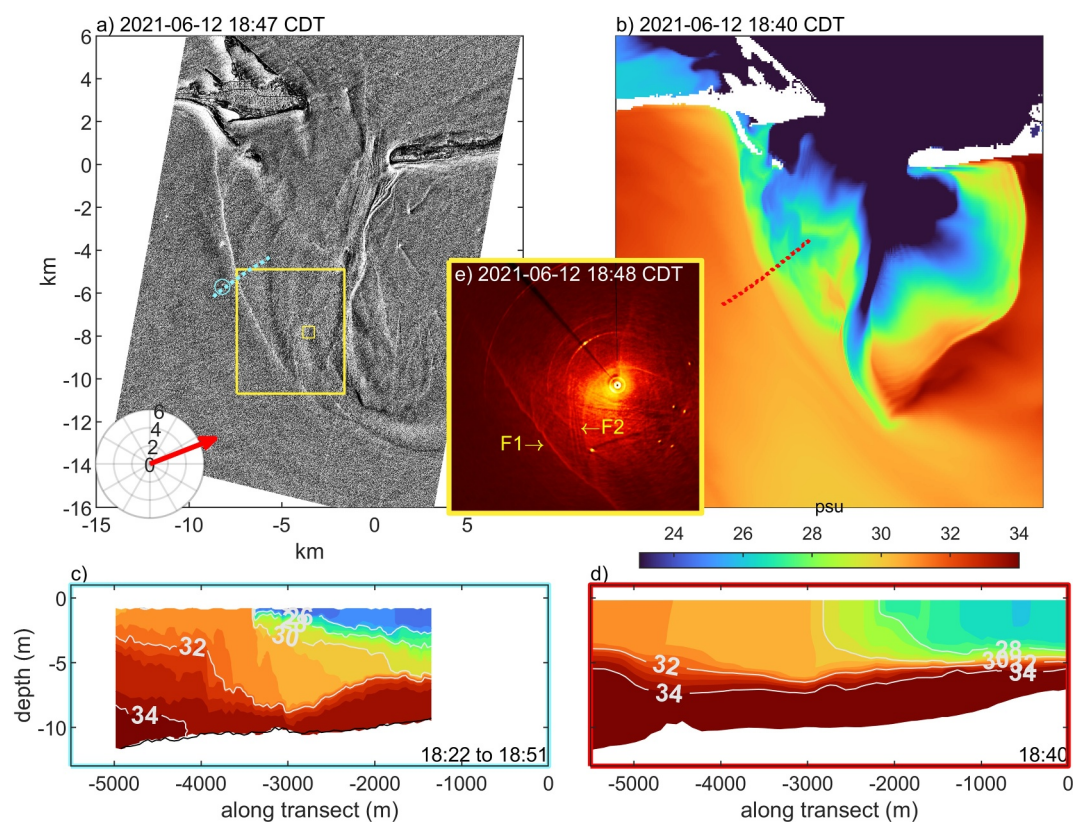
Figure 3. Observations and modeling of the plume front on June 12. (a) synthetic aperture radar image, marking location of transect data in (c) (blue line) and the *R/V Pelican* (blue circle) as well as the extent of X-band radar image in (e) (yellow box) and the location of the *R/V Point Sur* (yellow square); (b) surface salinity from the model with same axes as in (a), marking location of transect in (d); (c) shipboard transect of salinity; (d) corresponding salinity transect from model, with same axes as in (c); (e) shipboard X-band radar image, marking the main front (F1) and a secondary front (F2). Additional transect data, radar images, and model output are in Supporting Information S1.

R/V Point Sur was positioned closer to it (see Supporting Information S1). The surface expression of the bore is not obvious in the SAR image, although there is a change in image brightness about 600 m seaward of the plume front that roughly lines up with bore. Shipboard transects and radar images prior to the example in Figure 3 followed the plume front and subsurface bore as they moved seaward (see Supporting Information S1).

Model results corresponding to the time of the SAR image and shipboard transect illustrate similarities in the structure and propagation of the plume as well as differences. The surface salinity in the model (Figure 3b) shows the plume with a similar spatial structure as the bright front in the SAR image (Figure 3a). The ambient waters offshore in the model are stratified with similar total surface-to-bottom salinity difference (Figure 3d), but in the model the ambient pycnocline is sharper than in the observations (Figure 3c). The model has a subsurface perturbation to the pycnocline that propagates offshore like the bore in the observations, but it is shifted in location (e.g., at −4,800 m in transect in Figure 3d; see Supporting Information S1 for other examples). The similarities with the observations suggest common generation mechanisms for the bore, albeit with differences in timing and/ or propagation speed. The surface plume front follows and overtakes the subsurface bore in both the model and the observations. The vertical extent of the plume in the model is similar to the observations (2–3 m), although the plume thins more in the observations as it spreads offshore. The near-surface salinity in the model is greater than observed and thus the horizontal surface salinity gradient is weaker. Mean propagation speeds of the plume front during this period (e.g., following the 30 psu isohaline) are similar in the model and shipboard observations at about 0.2 m/s.

In-situ observations are limited to the June cruise period, but additional comparisons are made between SAR images and plume structure in the model. Model fields are plotted at the time closest to the SAR images, including
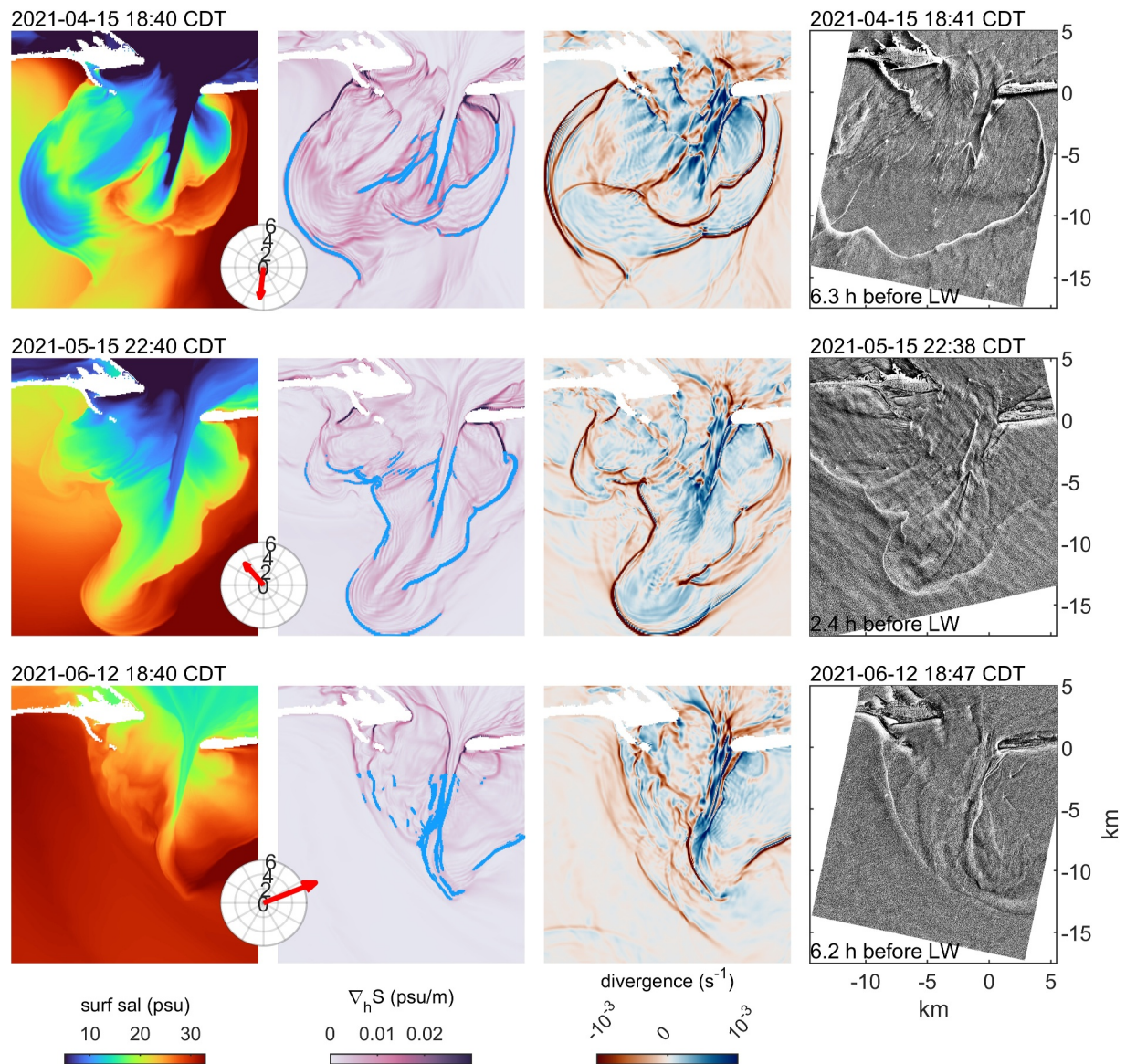
Figure 4. Examples of plumes under different forcing conditions, with modeled surface salinity (first column), surface salinity gradient ($\nabla_h S$, second column), surface divergence ($\partial u/\partial x + \partial v/\partial y$, third column), and observed synthetic aperture radar imagery (fourth column). Times shown are for plumes in April with northerly wind (top row), in May with southeasterly wind (middle row), and in June with southwesterly wind (bottom row), as in Figure 2. Light blue markers in the $\nabla_h S$ panels show the top 2% of strongest gradients used to characterize plume extent. Spatial extent is the same for all panels.

surface salinity, horizontal gradient of surface salinity ($\nabla_h S$), and surface velocity divergence (Figure 4). In the model the surface salinity gradient and velocity convergence are often co-located, with strong convergence (negative divergence) where $\nabla_h S$ is maximum. The model reproduces key aspects of the variability among the SAR images. Surface convergence is expected to be most correlated with SAR intensity because the convergence of small surface waves increases the radar cross-section. Convergences and surface salinity gradients are stronger in examples from April and May than in June, consistent with the brighter fronts in the SAR images. In April the modeled plume is relatively circular and symmetric about the mouth, in May there are multiple distinct lobes bending toward the west, and in June the western front is smoother and weakly defined, all like features in the SAR images.

The comparisons between the SAR images and the model are also notable for their differences. The plume fronts in the model do not appear as a single, clean front but instead have multiple lobes moving offshore in different directions and at different rates. The brightest regions in the SAR imagery are primarily related to the main plume
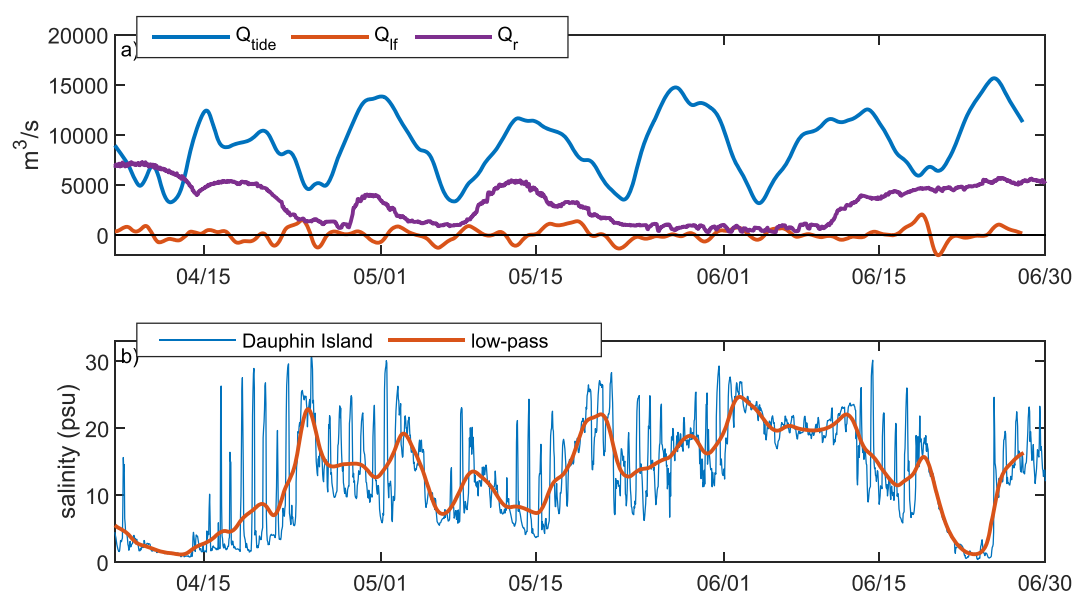
Figure 5. (a) Volume fluxes out of the estuary based on the observed tidal water level (Q_{tide}), subtidal (low-frequency) water level (Q_{lf}), the river discharge (Q_r); (b) observed tidal and subtidal salinity at Dauphin Island.

front, whereas the model shows multiple regions of enhanced convergence from secondary fronts that emerge after the main plume. The regions of enhanced velocity convergence associated with fixed bathymetric features in the model are consistent with the regions of persistently enhanced SAR backscatter, including over Sand Island shoals and at the edges of the navigation channel south of Fort Morgan. In these locations differential advection due to lateral shear in the outflow velocity creates lateral salinity gradients and baroclinic surface convergence. Additional comparisons between the model and observations are provided in Supporting Information S1.

Collectively, the comparison with observations provides support that the model is representing important aspects of the plume and its variability with forcing conditions. The general structure and location of the plume fronts and surface convergences correspond with frontal features in the SAR imagery, albeit with differences in the location and intensity. The model represents internal bores and plume fronts as they move offshore, and the plume thickness is similar to the observations. However, there are differences in the structure of the ambient and plume stratification that may relate to the differences in the location and intensity of the fronts. Uncertainty in initial and boundary conditions affect the ambient water properties and consequently plume propagation. The role of the wind and wind waves in mixing may not be well represented with the surface boundary parameterization for enhanced surface roughness (Carniel et al., 2009; Charnock, 1955). While the differences between modeled and observed conditions are a source of uncertainty, the differences in plume behavior owing to the forcing conditions are generally greater than the differences between the model and observations. In the next section, we use the model to quantify how tides, wind, and river discharge affect the plume.

3.2. Plume Variability With Forcing Conditions

The tidal amplitude, river discharge, and winds influence the size and location of the plume by affecting the volumetric tidal exchange and the dynamics of plume propagation. The tidal exchange estimated based on the water level fluctuations at the mouth and the surface area of the bay (100 km^2) varies by up to a factor of 3 between equatorial and tropic tides (Figure 5). The tidal fluxes through the mouth are 3–10 times greater than the river discharge during tropic tides, but during periods with high discharge and weak tides the river inputs are similar to the tidal exchange. The subtidal, low frequency water level associated with wind forcing causes volumetric exchange at time scales of several days that can be similar in magnitude to low river discharge. Note these estimated volume fluxes from observed water levels compare well with tidal and subtidal fluxes calculated from model results (not shown).

Observed near-surface salinity at Dauphin Island varied from less than 1 psu to more than 30 psu over the study period, with up to 25 psu variation within a tidal cycle (Figure 5). The river discharge is the primary influence on
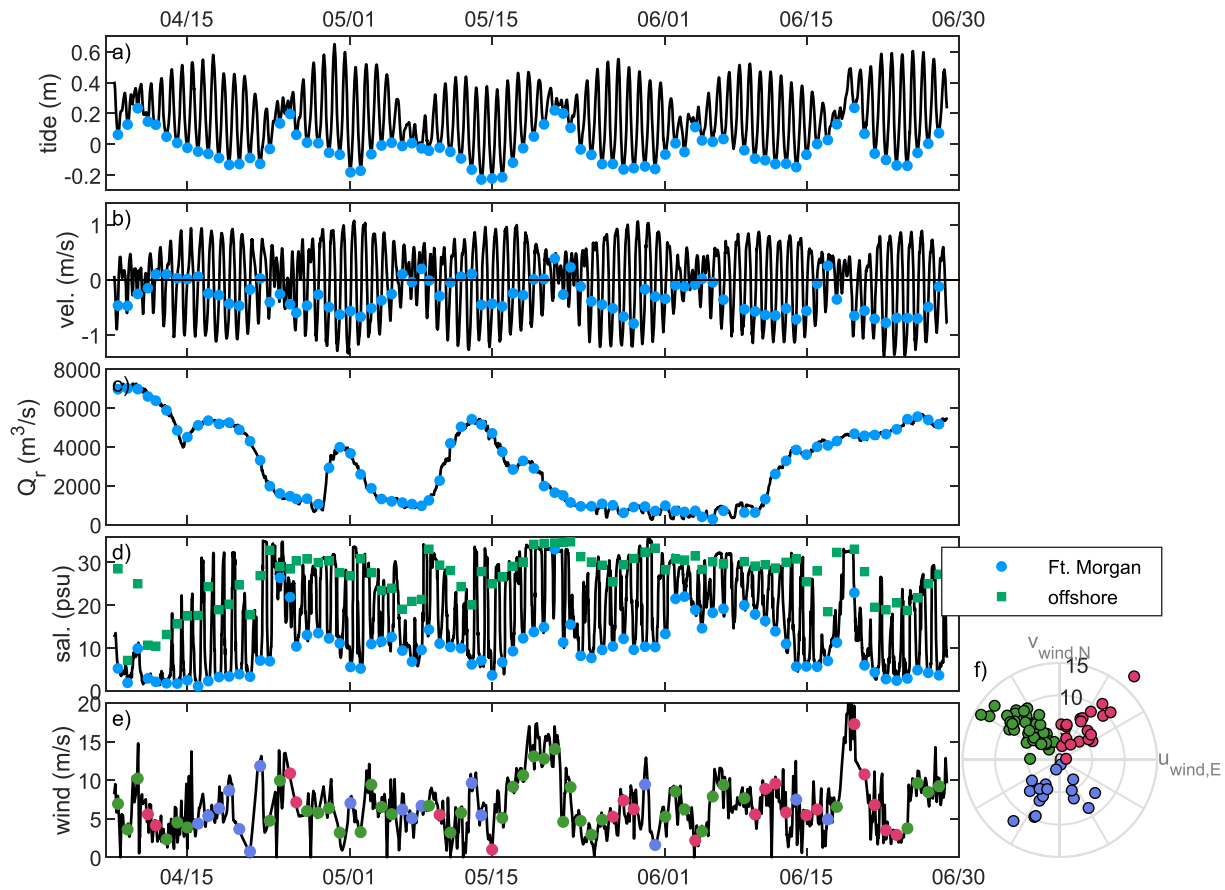
Figure 6. Forcing conditions for ebb plumes over the simulation period, noting with markers low tides when plume characteristics are compared in Figure 8 (*n* = 80). (a) Water level, (b) depth-average velocity at the mouth near Fort Morgan, (c) river discharge, (d) surface salinity at Fort Morgan (black line) along with average surface salinity offshore at the start of each ebb (green squares, averaging the surface salinity at the five locations along the 10-m isobath shown in Figure 1), (e) wind speed, and (f) wind vectors for ebb plumes (oceanographic convention, velocity toward). In (e) and (f) the markers are colored by wind direction as in Figures 8 and 9.

the subtidal variability with salinity generally decreasing following periods of higher discharge (Figure 5). However, shorter time scale fluctuations in salinity at the mouth correspond with the low-frequency water level due to upwelling and downwelling, as will be examined more later.

The nearly 3-month model simulation included 80 ebb plume realizations (Figure 6). Plumes were sampled at a consistent tidal phase of low tide for comparison. Low tide typically occurred about 5 hr after maximum ebb near Fort Morgan, so the plume snapshots corresponded with the end of ebb or beginning of flood tide (Figure 6b). The water column was stratified and highly sheared both in the navigation channel and offshore, so surface and bottom velocities often did not align. River discharge varied between 300 and 7,200 m^3/s (Figure 6c), diurnal tidal range was 0.08–0.8 m (Figure 6a), and wind speed was less than 1 m/s to more than 18 m/s (Figure 6e). The winds broadly fell into three categories: from the southeast, from the southwest, and from the north (Figure 6f). Surface salinity during the ebbs near Fort Morgan ranged from 2 psu to more than 20 psu (Figure 6d). Salinities offshore of the mouth also varied, from 7 psu to 35 psu. The difference between the salinity offshore and outflow at low tide increased with tidal amplitude, as fresher water from farther inside Mobile Bay reached the mouth during stronger ebb tides.

To diagnose the influences on the plume, we divide each of the forcing factors into range bins and compare conditions offshore of the mouth (Figure 7). The tide and discharge bin ranges are selected to have similar numbers of plume realizations over the simulation, and the wind is binned according to the dominant directions (from the SE, SW, and N). The forcing conditions are not correlated, as the river discharge is decoupled from the local wind forcing. The horizontal surface salinity gradient is shown as an indicator of plume position; however, the surface convergence has similar spatial patterns (Figure 4). In the bin averages by tidal range, the region with
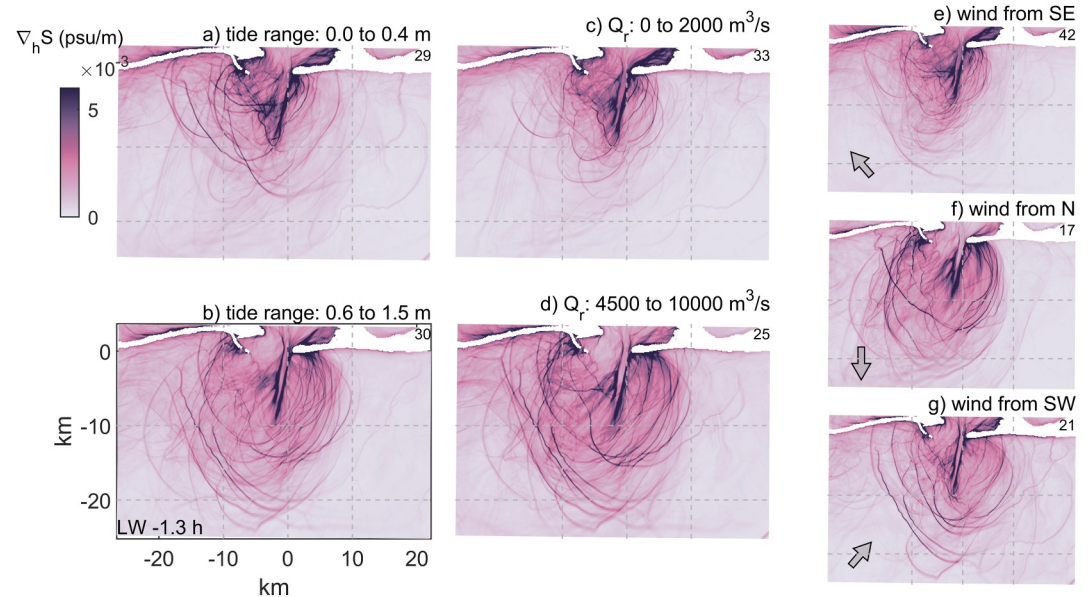
Figure 7. Bin-averaged surface salinity gradient for different tidal, river discharge, and wind conditions 1.3 hr before low water. Average conditions for (a) small (0.0–0.4 m) and (b) large (0.6–1.5 m) tidal ranges; for (c) low (0–2,000 m³/s) and (d) high (4,500–10,000 m³/s) discharge conditions; for wind (e) from the southeast, (f) from the north, and (g) from the southwest. The number of ebb tides averaged in each bin is shown in the upper right of each panel.

intensified salinity gradients moves farther offshore as the tidal amplitude increases (Figures 7a and 7b). Similarly, as river discharge increases, plume fronts move farther offshore (Figures 7c and 7d). Wind direction influences the location of the plume fronts as well as the intensities of the salinity gradients (Figures 7e and 7f). Wind from the southeast generally shifts plume fronts toward the west and winds from the southwest shift fronts 10–20 km east of the mouth. Winds from the southwest have intensified salinity gradients west of the mouth, which is consistent with increased convergence of wind-driven ambient currents in opposition to the spreading plume. Plume fronts with winds from the north tend to be farther offshore. Overall, plumes are often located southwest of the navigational channel, which is consistent with previous observations (Dinnel et al., 1990). Some regions with strong salinity gradients remain relatively fixed regardless of the forcing conditions, such as at the edge of the navigation channel due to lateral salinity gradients from differential advection, as noted in the SAR imagery (Figure 4).

To quantify the shifts in plume position with the forcing, the plume location is defined using a couple of approaches. First, plume location is defined based on a salinity anomaly relative to the ambient. However, because of the wide range of salinities in the outflow and offshore (Figure 6d), the plume cannot be specified based on a single isohaline through the study period. Instead, the plume extent is defined for each plume based on the isohaline midway between the average surface salinity offshore at the 10 m isobath at the start of the ebb and the minimum salinity in the outflow during that ebb. The mean position and total area of the plume are calculated as the region outside the mouth with surface salinity less than this isohaline. Alternatively, the tidal plume front is identified based on the location of strongest surface salinity gradient outside the mouth. The top 2% of the salinity gradients between model grid cells is chosen empirically based on the surface salinity maps (Figure 4 shows examples). Mean position of each plume front is calculated based on the average location of the strongest $\nabla_h S$, and plume area is calculated from the convex hull of those points. The examples illustrate some of the challenges of defining plume characteristics (Figure 4). The transition salinity between the outflow and the ambient increases from 15 psu to 22 psu to 28 psu in the three cases. The strongest $\nabla_h S$ generally maps out the extent of the main plume, but it also picks up regions in the plume interior where strong salinity gradients occur between lobes of outflow or surface fronts formed farther landward that emerge later in the ebb. However, generally the two approaches—based on surface salinity anomaly and surface salinity gradient—gave similar results for plume areas and position. The results presented here define plumes based on the surface salinity anomaly.
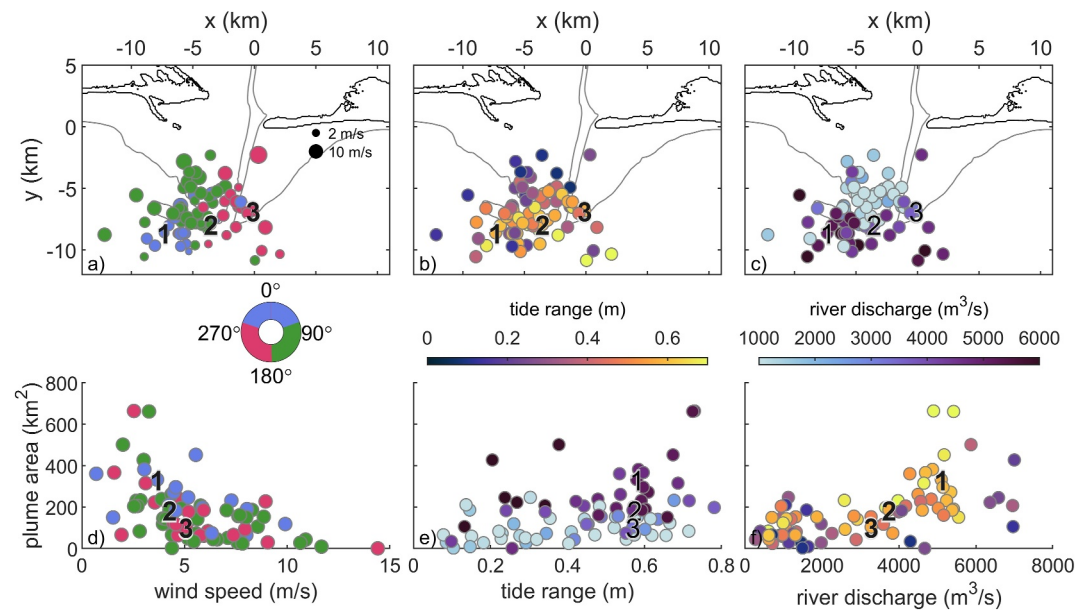
Figure 8. Plume front location (a–c) and plume area (d–f) at low tide depending on forcing. Mean location of the plume front based on the surface salinity anomaly, with (a) marker color based on wind direction and magnitude (marker size); (b) marker color based on tide range, (c) marker color based on river discharge. (d–f) Plume area versus (d) wind-speed (color for direction from), (e) tide range (color for discharge), and (f) river discharge (color for tide range). Labeled numbers correspond with plumes at low tide for the ebbs shown in Figure 4: 1 = April 15, 2 = May 15, 3 = June 12.

The mean position and plume area for the 80 plumes at low tide are plotted by forcing conditions: wind speed and direction, tidal range, and river discharge (Figure 8). The mean position of the plume tends to be southwest of the mouth, but both the along-shore (east-west) and cross-shore (north-south) position vary by more than 10 km. The east-west spread in plume position depends largely on the wind, with winds from the southeast shifting the plume west and winds from the southwest moving the mean position to the east (Figure 8a). The east component of the wind correlates with east-west position of the plume ($r^2 = 0.35$; all reported correlations are significant with $p < 0.001$). Alternatively, mean plume position can be calculated in radial coordinates from an origin at the mouth, and in that frame the east wind correlates with a shift in azimuthal position ($r^2 = 0.60$). Northerly wind tends to shift the plume offshore, albeit with a lower correlation for north-south ($r^2 = 0.16$) or radial ($r^2 = 0.15$) position. As suggested in the bin-averaged plots (Figure 7), increasing tidal range and river discharge both tend to shift the plume offshore (Figures 8b and 8c). Tidal water level range correlates with north-south position of the plume ($r^2 = 0.19$), and river discharge correlates with more southerly position ($r^2 = 0.26$) and increased radius ($r^2 = 0.26$).

Plume area at this tidal phase varies from about 100 km^2 to more than 500 km^2, increasing with river discharge ($r^2 = 0.36$) and tidal amplitude ($r^2 = 0.16$) (Figures 8e and 8f). The two factors are additive in that for a given tidal range (or river discharge) the plume area can increase by a factor of 2 or more depending on the river discharge (or tidal range). Plume size generally decreases with wind speed, but the correlation is weaker than the other factors ($r^2 = 0.11$). The correlations of plume area with the along-shore and across-shore components of the wind were similarly modest. Previous studies have found plume areas influenced by offshore expansion with upwelling and shoreward compression with downwelling (Dzwonkowski et al., 2015; Lentz, 2004; Whitney & Garvine, 2005), but that was not apparent in these results.

4. Analysis

4.1. Plume Front Propagation

Shifts in plume position depend on frontal propagation with the forcing conditions, and the velocity of the front depends on plume characteristics as well as the ambient conditions. The net frontal velocity is the sum of the gravity current speed and any ambient currents into which the front is propagating. We assess the influences of the
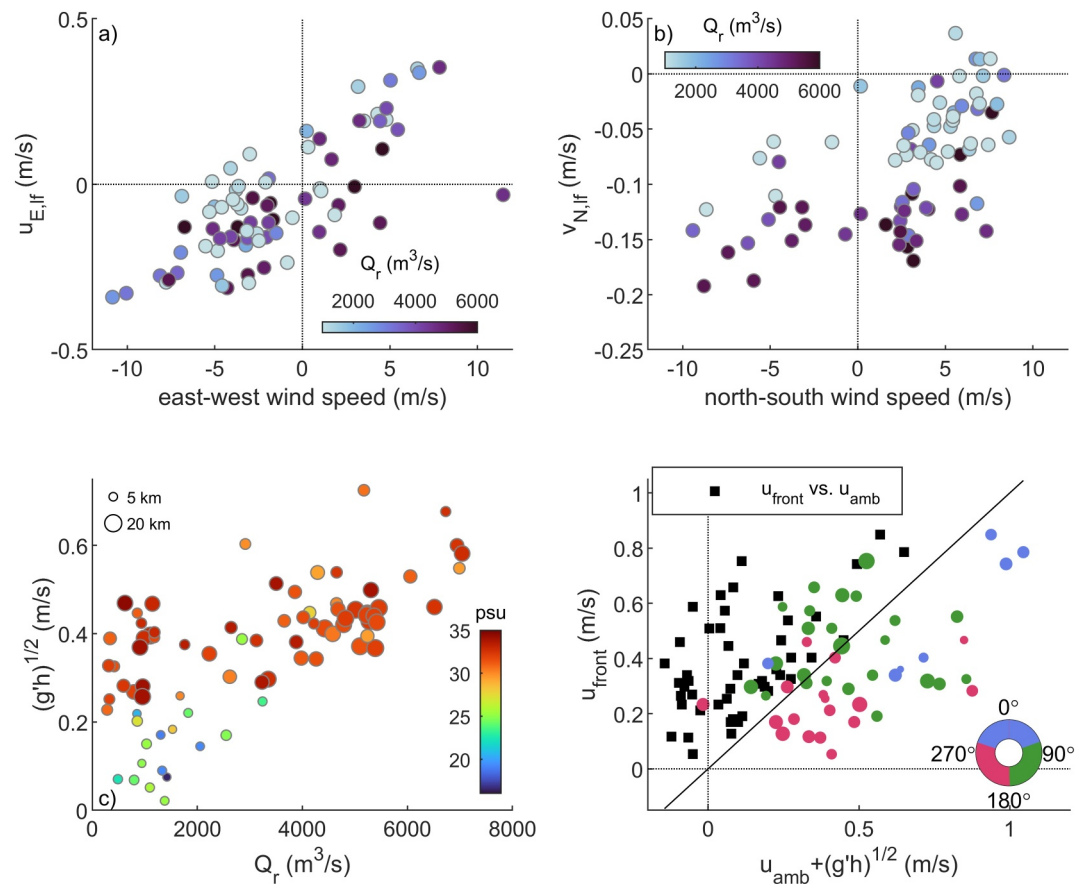
Figure 9. Velocity components influencing plume front propagation and forcing factors. (a) East component of low-pass filtered ambient surface velocities near 10-m isobath (see Figure 1 for locations) versus east-wind speed (markers colored by river discharge); (b) north component of low-pass filtered ambient surface velocities near 10-m isobath versus north wind speed (markers colored by river discharge); (c) $(g'h)^{1/2}$ of plume along western transect versus river discharge (marker color shows salinity of lower layer, marker size is scaled with distance offshore of plume front); (d) frontal propagation speed (u_{front}) versus the ambient velocity (u_{amb}) plus $(g'h)^{1/2}$ (colored markers, color shows wind direction) and u_{front} versus u_{amb} (black squares).

tides, winds, and river discharge on the velocity components contributing to plume front propagation and relate that to the variability in the plume location and size.

The strongest sources of variability in the near-surface ambient currents are the tides and the wind. Depth-averaged currents at maximum ebb in the navigational channel vary from 0.3 to 1.4 m/s, with the diurnal constituents representing more than 90% of the variance (Figure 6b). The tides dominate the volumetric exchange at the mouth, and river discharge has a minor influence on the outflow (Figure 5). Tidal velocities decrease as the outflow spreads offshore, and the influence of the winds increases. Harmonic analysis of the surface currents at the 10-m isobath shows that the main diurnal constituents (K1 and O1) have a total semi-major axis current amplitude of 0.3–0.4 m/s (Figure 1). However, the tidal constituents account for only about 30% of the near-surface velocity variance, and much of the rest is due to the winds.

Offshore of the mouth, the wind strongly influences the surface currents. At the 10-m isobath, the east component of the low-pass filtered, near-surface velocity prior to the plume varies between −0.3 m/s and +0.4 m/s depending on the wind speed and direction (Figure 9a). The subtidal surface currents are in the direction of the wind, with southwesterly winds driving currents to the east and southeasterlies causing near-surface flow to the west. (Wind velocities are plotted in oceanographic convention, direction toward.) Previous studies have also found that the coastal currents are highly coherent with the along-shelf wind (Dzwonkowski & Park, 2012; Dzwonkowski et al., 2015). River discharge does not have a major influence on the east-west component of the ambient currents. Discharge does play a role in the north-south component of the ambient currents, along with the wind (Figure 9b).

The north component of the low-pass filtered surface current ranges from -0.2 to 0.05 m/s, with northerly wind and high discharge accounting for the most seaward subtidal currents. Within a subset of discharge conditions (e.g., higher or lower discharge), the wind accounts for about 0.1 m/s of variability in the north velocity. Previous studies have found that the estuarine outflow plays the leading role in the cross-shore transport (Dzwonkowski & Park, 2012; Dzwonkowski et al., 2015), but in the nearshore region examined here the cross-shore wind has a similar influence.

The propagation speed of the front relative to the ambient currents depends on the density difference between the plume and the ambient waters, and both vary considerably (Figure 6). The characteristic speed of a gravity current depends on the density anomaly and the plume thickness as $\sqrt{g'h_p}$, where $g' = g(\rho_a - \rho_p)/\rho_a$ is the reduced gravity, ρ_p is the plume density, ρ_a is the density of the ambient, g is gravitational acceleration, and h_p is the plume thickness. The intrinsic propagation speed (u_i), or speed relative to the ambient, also depends on the plume thickness and the water depth (H). The analytical solution for a gravity current balancing inertia and the baroclinic pressure gradient results in an internal Froude number $Fr = u_i/\sqrt{g'h_p}$ that varies between $\sqrt{2}$ for a thin plume relative to the water depth ($H >> h_p$) and $Fr = 0.5$ for a plume that is half the water depth, or $h_p/H = 0.5$ (Benjamin, 1968). Typical values for h_p/H in this study are 0.1–0.4, corresponding to Fr between 1.2 and 0.8.

We use $\sqrt{g'h_p}$ as a characteristic velocity for the influence of buoyancy on plume front propagation. To quantify $\sqrt{g'h_p}$, a transect is defined on the west side of the mouth (Figure 1) oriented in the direction of typical plume propagation. The transect overlaps with the shipboard surveys (Figure 3) but extends farther seaward and landward. Model data are extracted along the transect for each ebb at low tide. Front position along the transect is identified based on the maximum near-surface salinity gradient. Plume thickness is calculated as the depth of the isohaline midway between the maximum and minimum salinity at each location along the transect, and average salinities are calculated for the upper and lower layers to estimate g'. The plume front location along the transect varied between 5 and 20 km with a mean of 12 km. Plume thickness had a relatively narrow range, with a mean of 1.9 m and standard deviation of 0.7 m. Plume thickness in this region is limited by the flow over the Sand Island shoals, which are 2.5–3 m deep. Plume thickness did not consistently vary with distance offshore in this region, but h_p/H decreased as the plume moved into deeper water from around 0.5 to 0.08.

The calculated $\sqrt{g'h_p}$ values were typically 0.2–0.5 m/s and increased during higher discharge periods (Figure 9c). Upper layer salinity decreased as the discharge increased, averaging 23 psu for $Q_r < 1,000$ m³/s and 9 psu for $Q_r > 6,000$ m³/s. Lower layer salinity was usually in the range of 30–35 psu with some exceptions during low discharge when the lower layer was fresher. For lower discharge cases, the spread in $\sqrt{g'h_p}$ depended primarily on the ambient, lower layer salinity. Cases with lower ambient salinity and reduced g' had fronts that remained relatively close to the mouth (Figure 9c), and in general the plumes during low discharge periods were not sharply defined. Previous observations have suggested a transition in the stratification conditions inside the estuary at around 3,000 m³/s (Noble et al., 1996), which could influence the buoyancy anomaly and the trends in plume size with discharge (Figure 8).

Plume front propagation speed (u_{front}) is calculated from the difference in front location along the transect over 80-min intervals. Calculated frontal speeds ranged from 0.1 to 0.8 m/s (Figure 9d). The spatial structure of the plume varied substantially day-to-day (e.g., Figure 4), and diagnosing the frontal propagation along a fixed transect is a simplification necessary to use the same approach for all the cases. The frontal propagation speed is compared with the ambient currents (u_{amb}) by extracting the near-surface velocities oriented along the transect just offshore of the front. Ambient currents near the front ranged from -0.2 m/s (i.e., opposing frontal propagation) to 0.6 m/s (Figure 9d). The frontal propagation speed depended on the ambient currents (black squares in Figure 9d) but adding the buoyancy velocity $\sqrt{g'h_p}$ to the ambient currents was a better predictor of the propagation speed than the ambient currents alone (Figure 9d, mean error of 0.09 m/s vs. -0.27 m/s). The discrepancy between $u_{amb} + \sqrt{g'h_p}$ and the calculated frontal speed depended on wind direction (Figure 9d), which likely reflects limitations in projecting the complex plume structure onto a fixed transect. Broadly, the analysis suggests

that plume front propagation depends on both the ambient currents and the buoyancy anomaly, and that Froude numbers are around 1. Detailed diagnosis of the plume front propagation is left for future work.

The variability in the ambient currents and the buoyancy anomaly helps to explain the temporal variation in the mean location of the plume. The east-west location of the plume depends primarily on the east component of the wind through the subtidal along-shore current. The plume front typically emerges over the shoals about 8 hr before low tide, so the ± 0.3 m/s in ambient currents due to the along-shore wind corresponds to a shift in the plume front of about 10 km, similar to the east-west distribution of plume location (Figure 8). The offshore extent of the plume depends on the range of variability in tidal velocities (~ 0.3 m/s), the low-frequency currents due to the north-south wind and river outflow (~ 0.1 m/s), and the buoyancy anomaly (~ 0.2 m/s). Similarly, this variability results in cross-shore variability in plume front position at low tide of around 10 km. These estimates of the amplitude of the influence of forcing factors on plume propagation do not consider time dependence in the ambient currents or buoyancy anomaly as the plume moves offshore, but they do help illustrate that the tides, wind, and river discharge all contribute significantly to the observed variability.

4.2. Freshwater Distribution

The variability in $\sqrt{g' h_p}$ depends on the river discharge but also on the influence of the wind on the outflow and ambient salinities. The time series of observed salinity at Dauphin Island illustrates the multiple factors (Figure 5). While the salinity at the mouth generally decreases during periods of higher discharge, some of the sharpest changes correspond with water level set-up or set-down at the coast. For example, rapid increases in salinity occurred during periods of across-shore set-up of ~ 0.2 m (e.g., 24 April, 03 May, 19 May). Midway through a 2-week period of relatively high discharge when the outflow salinity was steadily declining, passage of a storm (19 June, Tropical Storm Claudette to the west) caused a coastal setup that increased salinity by a few psu and then a set-down that decreased salinity by more than 10 psu. Water level response to along-shelf winds was consistent with coastal Ekman (Dzwonkowski & Park, 2012; Kim & Park, 2012; Schroeder & Wiseman, 1985). Easterly winds drive coastal setup and transport higher salinity water into Mobile Bay, particularly with low discharge and weak stratification (Kim & Park, 2012). In one example, persistent wind from the east/southeast from a tropical storm increased salinity inside Mobile Bay by 8 psu above normal (Cambazoglu et al., 2017). The volumetric exchange with the subtidal water level is small compared to the tides or river (Figure 5), but the wind-driven setup and set-down influence salinity at the mouth and therefore plume propagation.

The plume characteristics fit within the broader context of how freshwater is distributed from the estuary to coastal ocean. The model results are used to quantify the freshwater content based on the salinity anomaly relative to offshore. In Upper Mobile Bay (>20 km north of the mouth), the freshwater content is highly correlated with river discharge ($r^2 = 0.63$) and weakly correlated with the tides ($r^2 = 0.20$), with more freshwater during tropic tides when up-estuary salt flux from the estuarine circulation decreases (Kim & Park, 2012). In Lower Mobile Bay, freshwater content also increases with discharge ($r^2 = 0.88$), but with a lag of several days from the inflow at the head of the bay. In the region offshore of the mouth (within 25 km), multiple factors have similar levels of influence. Freshwater content increases with discharge ($r^2 = 0.45$), during tropic tides when plumes are bigger ($r^2 = 0.35$), with upwelling winds that bring more freshwater out Main Pass ($r^2 = 0.44$ with 1–2 days lag), and with decreased salinity at the offshore boundary ($r^2 = 0.36$). The first three of these factors are related to increased transport from Mobile Bay to the Gulf; the last is related to the freshwater content of the regional coastal waters. The subtidal freshwater content varies more slowly than individual plumes, but it illustrates how the competing factors collectively influence water properties near the mouth.

4.3. Constant Wind Forcing Model Scenarios

The wind forcing affects plume propagation through modification of the ambient currents, the ambient salinity, and the salinity of the outflow (Figure 9). To diagnose the distinct contributions of the wind, we use idealized modeling experiments with constant wind forcing. These simulations focus on the early June period of in-situ observations, and use the same realistic forcing for the tides, river discharge, and other boundary conditions. Idealized winds are held steady at 4 m/s as a representative moderate velocity, and scenarios are run for winds from the southwest, from the north, and from the southeast.
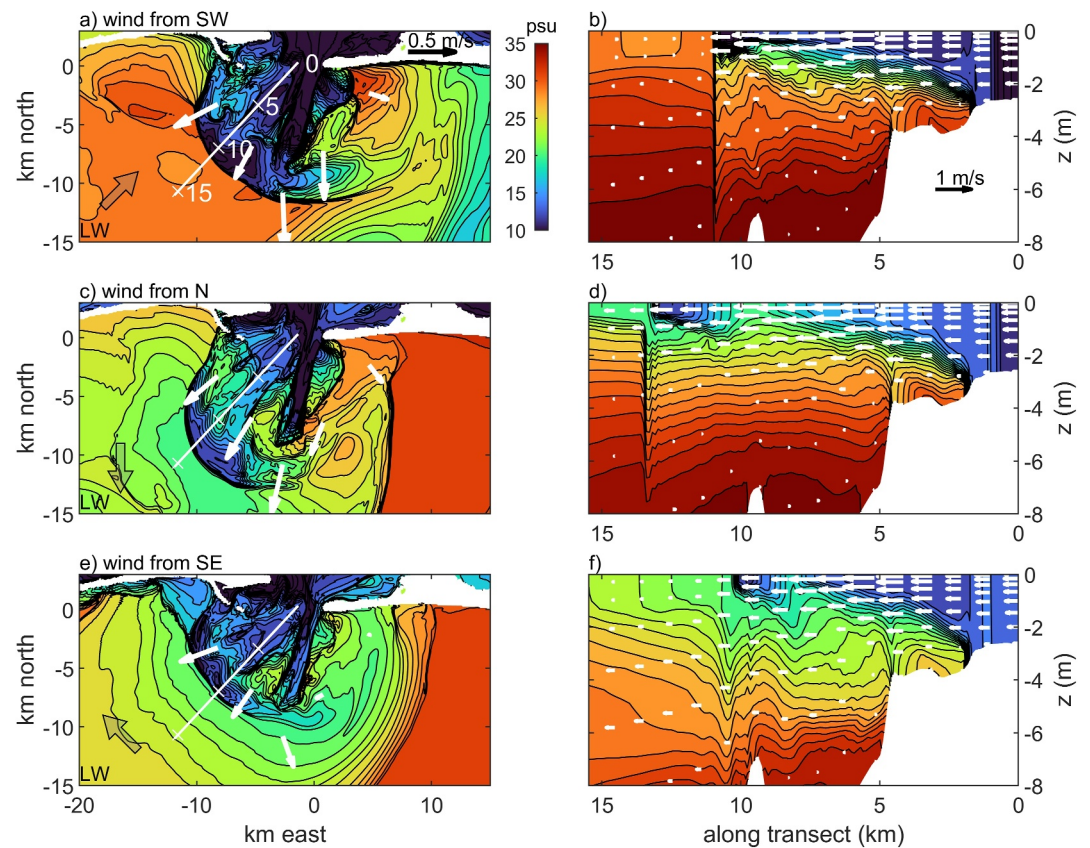
Figure 10. Snapshots of the plume under steady wind forcing, with map views (left panels) and transect profiles (right) at low water. (a and b) Wind from the southwest; (c and d) wind from the north; and (e and f) wind from the southeast. Transect location shown on the map view. White arrows in the left panels represent near-surface velocities, and gray arrows indicate wind direction.

Comparison of the idealized cases shows that wind can substantially alter the salinity inside the estuary and the freshwater discharge from the outlets. Wind from the southwest pushes fresher water toward the east in Mobile Bay and the freshwater transport occurs predominantly out the navigation channel. For example, at the 10-m isobath outside the mouth more than 90% of the total freshwater flux discharges in the navigational channel and eastward in the steady southwest wind case. With wind from the southeast or north, more of the freshwater outflow goes over the Sand Island shoals and the freshwater flux is more evenly distributed to the east and west of the navigation channel. Southeasterly wind also sends more freshwater outflow through Pass-aux-Heron to Mississippi Sound rather than out Main Pass with the plume. With the steady southeasterly wind, the average freshwater flux to Mississippi Sound is about 1/3rd of the total river input compared with just a few percent for southwesterly or northerly wind. A previous study also found the freshwater outflow was sensitive to the wind, albeit with different forcing—wind from due east shifted about 90% of river input to Pass-aux-Herons, compared with winds from due west that caused import of freshwater through Pass-aux-Herons and export through Main Pass (Du et al., 2018). Thus, the influence of the wind direction on the salinity inside Mobile Bay affects the plume in a couple of ways. Southeasterly winds reduce the freshwater flux out of Main Pass and shift a greater fraction of the outflow toward the western shoals where mixing is enhanced by shallow bathymetry. Southwesterly winds are associated with an outflow that is fresher and more focused in the deep navigational channel where there is less mixing by bottom-generated turbulence to increase the salinity of the plume.

Wind direction also influences the ambient salinity into which the plume propagates (Figure 10). Southwesterly winds cause upwelling that increases the lower layer salinity and transports previous plumes offshore. The upwelling of saltier water and export of previous plumes increase the buoyancy anomaly with southwesterly wind compared to the southeasterly or northerly wind (Figure 10). With southeasterly wind, the along-shore current retains previous plumes near the mouth and additional freshwater emerges onto the shelf through Petit Bois Pass
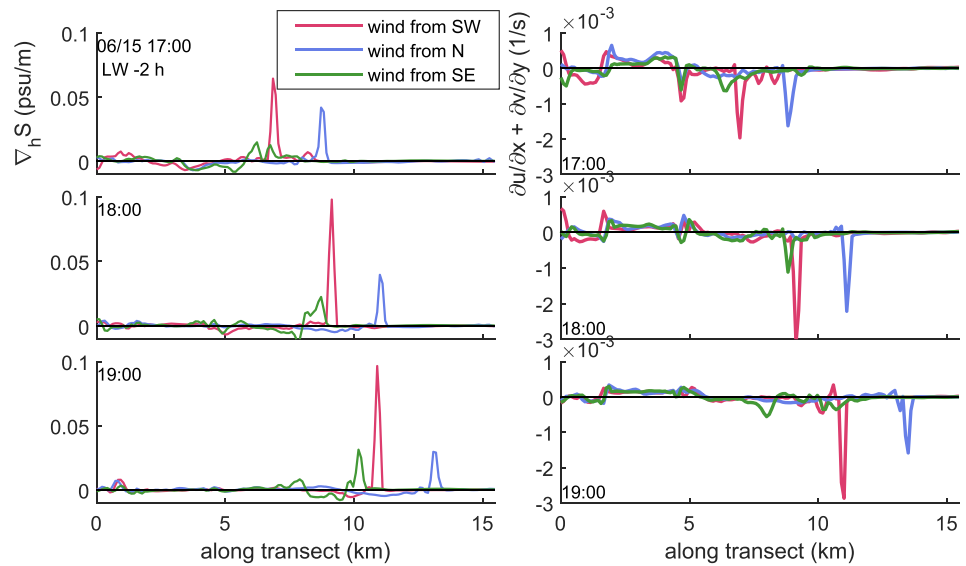
Figure 11. Surface salinity gradient (left column) and surface velocity divergence (right) for the steady wind forcing cases at three times during the ebb along the transect shown in Figure 10: 2 hr before low water, 1 hr before low water, and low water.

(Figure 1). This causes overall freshening of the ambient salinity compared to the southwesterly wind, reducing the buoyancy anomaly of plumes.

The combined influences of the winds on the ambient currents and salinity and the outflow salinity affect how plumes propagate offshore (Figure 10). We examine the salinity gradient and horizontal velocity convergence along the transect west of the mouth. In all the wind cases, the strongest salinity gradient and strongest convergence align, and their magnitudes are roughly proportional. The front is strongest for the southwesterly (upwelling) wind scenario, with a surface salinity gradient of 0.05–0.1 psu/m and velocity convergence of 2–3×10^{-3} s^{-1} (Figure 11). The salinity gradient is enhanced due to the fresher outflow through Main Pass (relative to other wind conditions) and saltier ambient with upwelling. The convergence on the west side is also enhanced by the ambient wind-driven currents that oppose plume propagation, causing downwelling at the front and depression of isopycnals almost 10 m below the surface (Figure 10b). The front in northerly wind case is weaker and farther offshore due to the wind enhancing near-surface velocities (Figures 10c and 10d). Northerly winds also accelerate transport of the fresh surface layer through the estuary (Du et al., 2018; Noble et al., 1996), decreasing the outflow salinity compared to the other wind cases. With the southeasterly (downwelling) wind (Figures 10e and 10f), the plume is saltier and the ambient is fresher such that the salinity gradient at the front is 3–5 times less than with southwesterly (upwelling) wind (Figures 10a and 10b). Weaker salinity gradients and wind-driven currents toward the west decrease the velocity convergence by an order of magnitude compared with the southwesterly wind case (Figure 11).

While the idealized scenarios are useful for diagnosing wind influences on plume propagation, it is important to keep in mind that the synoptic time scales of wind variability are shorter than the 10-day simulation period with steady wind forcing examined here. The realistic forcing has variability in the outflow salinity with wind direction that is consistent with the lateral shifts in freshwater near the mouth in the idealized cases. However, differences in the ambient salinity between upwelling and downwelling in the steady wind cases (Figure 10) are not as apparent in the realistic forcing. This is likely due to the relatively long time scales for the coastal Ekman transport to spin-up and alter the salinity through upwelling and cross-shelf transport compared to the wind variability. Observational studies with moorings offshore of Mobile Bay have found that the ambient salinity and currents depend on the along-shore wind (Dzwonkowski & Park, 2012; Dzwonkowski et al., 2014) similar to patterns in the idealized wind model results, but the effects are amplified by the sustained, steady forcing in the simulations.

5. Discussion

5.1. Context From Other Plume Studies

Several characteristics make the coastal Gulf of Mexico distinctive compared to other coastal regions, including the dominance of diurnal tides, a wide shelf with strongly wind-driven currents, and multiple large freshwater inputs. Previous studies of the Mobile Bay plume found that plume size was linked to river discharge and tidal amplitude (Dinnel et al., 1990; Stumpf et al., 1993), and the plume position responded rapidly to wind forcing (Dinnel et al., 1990; Dzwonkowski et al., 2015; Stumpf et al., 1993). The mean plume size from 33 Landsat images over 11 years of around 400 km^2 was similar to the results here (Figure 8), although the range in that study was greater (63–1,722 km^2), perhaps due to tidal phase variability in the observations (Dinnel et al., 1990). As in the idealized wind scenarios here, mooring observations on the shelf showed the western expansion of the plume front encountering eastward ambient currents during upwelling winds (Dzwonkowski et al., 2015). Studies of smaller scale plumes along the Gulf Coast identified features that are consistent with the Mobile Bay results. The Choctawhatchee River plume also varies in size predominantly with tidal amplitude and shifts in along-shore position with upwelling or downwelling winds (Cyriac et al., 2020; Huguenard et al., 2020). In SAR images of small-scale plumes on the Louisiana shelf, fronts were intensified on the western side due to convergence with ambient currents under upwelling winds (Li et al., 2017). The wind response of the Mobile Bay plume is consistent with Perdido Estuary plume, a neighboring small-scale system in the Mississippi Bight, in that wind forcing acts both directly on plume and on the estuarine outflow (Xia et al., 2011).

The diurnal tides, river discharge events, and synoptic winds over a stratified shelf all affect the plume at spatial scales of tens of km and time scales of days. The overlapping influences contrast with the conceptual framework that breaks plume evolution into spatially and temporally distinct dynamical regions: a near-field plume where the momentum from the tides and river discharge are the primary factors, the mid-field or recirculating plume where Coriolis and buoyancy dominate, and the far-field where a coastal current depends on rotation, the cross-shore pressure gradient, and the wind (Horner-Devine et al., 2015). The results here do not show distinct separation between dynamical regions. Instead, the diurnal tides and fluctuations in river discharge expand the near-field so that it overlaps with the mid-field, the wind-driven currents in the mid-field have greater influence than rotation, and collectively the forcing variability inhibits establishment of a far-field coastal current.

In a previous study, ocean color images of the Mobile Bay plume over several days of relatively weak winds and high river discharge suggested growth of a large, anti-cyclonic bulge to the west of the mouth (Dzwonkowski et al., 2015). However, a recirculating bulge region was not apparent in the model or SAR imagery in this study. Instead, the tides and wind dominated the mid-field structure. The diurnal tropic tides result in offshore excursions of the plume (~20 km) that greatly exceed the deformation scale (~5 km = $(g'h_p)^{1/2}/f$, where f is the Coriolis parameter, 7.29×10^{-5} rad/s at 30°N). The along-shore tidal current near the mouth is about half the amplitude of the across-shore (Figure 1), and when plumes are discharging the ambient tidal flow is westward. Additionally, the wind-driven along-shore currents can be comparable to the tides (Figure 9) and last for hours to days, reinforcing or opposing tidal advection depending on wind direction. Other observations of plumes from Mobile Bay and the nearby Choctawhatchee River also show strong dependence on the wind rather than persistent, geostrophic features (Gelfenbaum & Stumpf, 1993; Roth et al., 2017).

The satellite images of the bulge outside Mobile Bay occurred during a prolonged period with high discharge and anomalously low winds, with wind speeds less than about 4 m/s for 8 days (Dzwonkowski et al., 2015). Bulge formation requires multiple days of freshwater accumulation to be retained locally before flowing into a coastal current (Fong & Geyer, 2002; Horner-Devine et al., 2008). The magnitude and variability of plume advection due to tides and winds disrupts the bulge formation and blurs distinctions between the near-, mid- and far-field regions. For example, consider the dominant terms of the along-shore momentum budget. The tidal-band along-shore water level gradients ($\partial\eta/\partial y$) oscillate with a typical amplitude of around 0.5×10^{-3}. The subtidal, wind-driven gradients can be several times larger during big events. The along-shore pressure gradient term, $g\partial\eta/\partial y$, then is approximately 0.005 m/s^2. The Coriolis term, uf, using a nominal plume velocity u of 0.5 m/s, is 2 orders of magnitude smaller than the along-shore pressure gradient. The ambient currents offshore of Mobile Bay are not so large as to arrest plume propagation, as seen for plumes like the Connecticut River (Garvine, 1984; Honegger et al., 2024), but the diurnal tides and substantial wind contribution determine plume fate over relatively large spatial scales rather than dynamically shifting into geostrophic control and recirculation.

The Mobile Bay outflow ($\overline{Q_r} \approx 1{,}900$ m^3/s) has a large discharge but a shallow plume due to the flow over the ebb delta that limits plume thickness to just a few meters. The shallow plume, as well as the shallow stratification in the ambient, results in a rapid response of the surface currents to wind stress. Additionally, the diurnal time scale for the tidal plume of Mobile Bay, compared with the dominantly semi-diurnal forcing of many other systems, brings the tidal and meteorological time scales closer and increases the influence of the wind. Along-shore winds drive currents that are similar in magnitude to the offshore tidal currents and alter the trajectory of the tidal plume. Wind has been found to influence the near-field regions of other shallow plumes. For the Fraser River ($\overline{Q_r} \approx 3{,}500$ m^3/s) plume, the subtidal ambient surface currents are highly coherent with the wind (Halverson & Pawlowicz, 2016), and winds shift the along-shore position and surface convergence of the tidal plume front depending on direction (Kastner et al., 2018). The propagation speed and plume thickness of the Rhine River ($\overline{Q_r} \approx 2{,}900$ m^3/s) tidal plumes are also affected by wind-driven currents (Rijnsburger et al., 2018). The Merrimack River ($\overline{Q_r} \approx 200$ m^3/s) plume is smaller scale, and wind affects the tidal plume location, ambient salinity, and mixing at the front (Kakoulaki et al., 2014; Spicer et al., 2022). Propagation of the Connecticut River ($\overline{Q_r} \approx 400$ m^3/s) plume front depends primarily on the ambient tidal currents, but wind stress can alter the front speed by up to 30% through increased near-surface shear in the ambient velocities (Honegger et al., 2024). Across this wide range of discharge conditions, a common characteristic of these wind-influence tidal plumes is they are relatively shallow, with typical thickness of 2–4 m.

The observations and modeling of the Mobile Bay plume demonstrate overlapping influences of multiple forcing factors rather than distinct regimes with dominant dynamical balances. Laboratory or idealized numerical studies of plumes without tidal or wind-driven variability do not have this overlap, and therefore allow for clearer development of a bulge and coastal current (Fong & Geyer, 2002; Yuan et al., 2018). Forcing conditions for other plumes may also allow for more distinct separation among the regimes. For example, studies of the Columbia River plume have divided it into a tidal near-field with time scales of hours, a bulge recirculating over days, and along-coast transport at longer time scales (Hickey et al., 1998; Horner-Devine et al., 2009; Jay et al., 2009). The Columbia has mixed semi-diurnal tides, strongly seasonal river discharge and wind forcing, and a narrow, deep shelf. In contrast, Mobile Bay has dominantly diurnal tides and large tidal excursions (∼20 km), strong frontal winds on a stratified shelf, and river discharge that varies rapidly with precipitation events. The large-scale variability in the plume (tens of km) at short time scales (a few days) merges the near-field and mid-field regions, and this unsteadiness inhibits formation of a far-field coastal current. The multiple, interacting influences on other plumes noted above indicate that the dynamical messiness of Mobile Bay may be more common than not.

5.2. Remote Sensing of Plume Fronts

Satellite-based remote sensing is distinctive for synoptically characterizing features that are large-scale and rapidly evolving. Ocean color or reflectance can be indicative of plume water properties like turbidity or chlorophyll concentration, which often vary at seasonal time scales as seen in Mobile Bay (Dinnel et al., 1990; Dzwonkowski et al., 2015; Stumpf et al., 1993), the Columbia (Thomas & Weatherbee, 2006), and smaller coastal discharges (Piñones et al., 2005; Warrick et al., 2007). However, limitations such as revisit frequency, environmental artifacts like cloud-cover, and data access or acquisition costs make it challenging to use satellite data to diagnose processes at tidal or meteorological time scales.

SAR satellite imagery has the potential to provide quantitative information on the near-surface currents through the intensity of the radar backscatter. Analyses of SAR images of the Rhine plume were paired with a simplified, two-layer model of the currents to show that backscatter intensity increased in regions of the front with greater surface convergence (Hessner et al., 2001). However, asymmetries observed in-situ between upwelling or downwelling winds in convergence at the Columbia River plume front were not apparent in SAR imagery (Jay et al., 2009). Analyses of SAR images from Mobile Bay in this study indicate that the radar cross-section can be inverted for quantitative estimates of the surface convergence (Wackerman, 2023). The approach estimates radar cross-section as a function of the surface wavefield, and surface current gradients at the front are inferred from the differences between that and observed SAR imagery. Comparisons between convergences at plume fronts calculated from the SAR images and in the hydrodynamic model were favorable, although convergences were weaker in the model than the SAR due in part to grid resolution. Unfortunately, the frontal crossings in the shipboard surveys were not synced with the SAR images to permit direct comparisons of remote and in-situ measurements. The idealized wind cases showed that environmental conditions such as the ambient currents,

the ambient salinity, and the plume salinity strongly influence plume front convergence and suggest that the SAR imagery could provide information on water properties, particularly if coupled with other observations.

6. Summary

Satellite observations and realistic modeling indicate that the structure and size of the outflow plume from Mobile Bay is highly variable over a 3-month period in the spring of 2021. The plume area at the end of ebb tide varies by more than a factor of 5, and mean location of the plume front varies by more than 10 km in both the along-shore and across-shore directions (Figure 8). Here we find that the wind forcing has a similar level of influence as the tide and river discharge on the near-field plume conditions.

Distinct characteristics of the forcing influence the Mobile Bay plume. The tides are predominantly diurnal and microtidal (0.1–0.9 m), but the large surface area of the estuary results in large variations in tidal volume flux between equatorial and tropic tides (Figure 5). The freshwater input is one of the largest coastal discharges in the U.S. and changes rapidly with precipitation events and upstream flow regulation. Winds during the spring and summer vary in magnitude and direction with frontal passages and tropical storms. The diurnal tides make the dominant time scale of the tidal plume closer to the event time scales than would be the case for semi-diurnal tides. Along with time scales, the winds and tides have similar magnitudes of influence on the ambient currents affecting plume advection. Offshore of the mouth tidal currents reach ∼0.5 m/s during tropic tides and are negligible during the weakest equatorial tides. Stratification on the shelf makes the surface currents highly responsive to the wind such that the along-shore (east-west) component drives variability of around ± 0.4 m/s (Figure 9). Northerly winds contribute to the subtidal cross-shore ambient surface currents in a manner similar to the river discharge.

Propagation of the frontal plume boundaries also depends on the buoyancy anomaly, which has multiple sources of variability. Plume thickness is typically around 2 m because the outflow passes over shoals of the ebb tide delta. The shallow plume thickness makes it more responsive to direct wind forcing than would be expected for a large river outflow with a deeper sill. The salinity of the outflow decreases with river discharge overall, but lateral shifts in the salinity distribution within the estuary due to the wind affect the freshwater flux out the mouth. The along-shore wind also influences the buoyancy anomaly and plume propagation through changes in the ambient salinity. Upwelling (westerly) winds bring saltier water to the coast from deep and advect lower salinity water from previous plumes offshore, whereas downwelling (easterly) winds retain previous plumes near the mouth for longer. The combined influences of the wind on salinity both inside and outside the estuary make the plume fronts and velocity convergences stronger with upwelling winds than downwelling, although this was more apparent in idealized model results with steady winds than in the realistic simulations or the SAR imagery. Synoptic sampling from satellite imagery permitted evaluation of plume structure that would not have been possible from in-situ observations alone, and initial comparisons of surface convergence at plume fronts derived from the SAR data suggest promising new approaches for remote sensing of the coastal ocean.

Data Availability Statement

Data used in this study are available at https://doi.org/10.5281/zenodo.10659126 (Ralston, 2024). SAR imagery is available through the Woods Hole Open Data Access Server at https://hdl.handle.net/1912/67567 and https://doi.org/10.26025/1912/67567 (Ralston et al., 2024). ARCOS data are available at https://www.disl.edu/arcos/. The CTD data from Mobile Bay in 2019 are available through the Dauphin Island Data Management Center (https://data.disl.edu/) and have been submitted to the NOAA National Center for Environmental Information (NCEI).

References

Benjamin, T. B. (1968). Gravity currents and related phenomena. *Journal of Fluid Mechanics*, *31*(2), 209–248. https://doi.org/10.1017/s0022112068000133

Cambazoglu, M. K., Soto, I. M., Howden, S. D., Dzwonkowski, B., Fitzpatrick, P. J., Arnone, R. A., et al. (2017). Inflow of shelf waters into the Mississippi Sound and Mobile Bay estuaries in October 2015. *Journal of Applied Remote Sensing*, *11*(3), 032410. https://doi.org/10.1117/1.JRS.11.032410

Carniel, S., Warner, J. C., Chiggiato, J., & Sclavo, M. (2009). Investigating the impact of surface wave breaking on modeling the trajectories of drifters in the northern Adriatic Sea during a wind-storm event. *Ocean Modelling*, *30*(2–3), 225–239. https://doi.org/10.1016/j.ocemod.2009.07.001

Charnock, H. (1955). Wind stress on a water surface. *Quarterly Journal of the Royal Meteorological Society*, *81*(350), 639–640. https://doi.org/10.1002/qj.49708135027

Coogan, J., & Dzwonkowski, B. (2018). Observations of wind forcing effects on estuary length and salinity flux in a river-dominated, microtidal estuary, Mobile Bay, Alabama. *Journal of Physical Oceanography*, *48*(8), 1787–1802. https://doi.org/10.1175/JPO-D-17-0249.1

Coogan, J., Dzwonkowski, B., Lehrter, J., Park, K., & Collini, R. C. (2021). Observations of dissolved oxygen variability and physical drivers in a shallow highly stratified estuary. *Estuarine, Coastal and Shelf Science*, *259*, 107482. https://doi.org/10.1016/j.ecss.2021.107482

Cyriac, R., Dietrich, J. C., Blain, C. A., Dawson, C. N., Dresback, K. M., Fathi, A., et al. (2020). Wind and tide effects on the Choctawhatchee Bay plume and implications for surface transport at Destin Inlet. *Regional Studies in Marine Science*, *35*, 101131. https://doi.org/10.1016/j.rsma.2020.101131

Dinnel, S. P., Schroeder, W. W., & Wiseman, W. J. (1990). Estuarine-shelf exchange using landsat images of discharge plumes. *Journal of Coastal Research*, *6*, 789–799.

Du, J., Park, K., Shen, J., Dzwonkowski, B., Yu, X., & Yoon, B. I. (2018). Role of baroclinic processes on flushing characteristics in a highly stratified estuarine system, Mobile Bay, Alabama. *Journal of Geophysical Research: Oceans*, *123*(7), 4518–4537. https://doi.org/10.1029/2018JC013855

Dykstra, S. L., & Dzwonkowski, B. (2020). The propagation of fluvial flood waves through a backwater-estuarine environment. *Water Resources Research*, *56*(2), e2019WR025743. https://doi.org/10.1029/2019WR025743

Dzwonkowski, B., & Park, K. (2012). Subtidal circulation on the Alabama shelf during the Deepwater Horizon oil spill. *Journal of Geophysical Research*, *117*(C3), C03027. https://doi.org/10.1029/2011JC007664

Dzwonkowski, B., Park, K., & Collini, R. (2015). The coupled estuarine-shelf response of a river-dominated system during the transition from low to high discharge. *Journal of Geophysical Research: Oceans*, *120*(9), 6145–6163. https://doi.org/10.1002/2015JC010714

Dzwonkowski, B., Park, K., & Jiang, L. (2011). Subtidal across-shelf velocity structure and surface transport effectiveness on the Alabama shelf of the northeastern Gulf of Mexico. *Journal of Geophysical Research*, *116*(C10), C10012. https://doi.org/10.1029/2011JC007188

Dzwonkowski, B., Park, K., Kyung Ha, H., Graham, W. M., Hernandez, F. J., & Powers, S. P. (2011). Hydrographic variability on a coastal shelf directly influenced by estuarine outflow. *Continental Shelf Research*, *31*(9), 939–950. https://doi.org/10.1016/j.csr.2011.03.001

Dzwonkowski, B., Park, K., Lee, J., Webb, B. M., & Valle-Levinson, A. (2014). Spatial variability of flow over a river-influenced inner shelf in coastal Alabama during spring. *Continental Shelf Research*, *74*, 25–34. https://doi.org/10.1016/j.csr.2013.12.005

Fong, D. A., & Geyer, W. R. (2002). The alongshore transport of freshwater in a surface-trapped river plume. *Journal of Physical Oceanography*, *32*(3), 957–972. https://doi.org/10.1175/1520-0485(2002)032<0957:TATOFI>2.0.CO;2

Garvine, R. W. (1974). Dynamics of small-scale oceanic fronts. *Journal of Physical Oceanography*, *4*, 557–569. https://doi.org/10.1175/1520-0485(1974)004<0557:dossof>2.0.co;2

Garvine, R. W. (1984). Radial spreading of buoyant, surface plumes in coastal waters. *Journal of Geophysical Research*, *89*(C2), 1989–1996. https://doi.org/10.1029/jc089ic02p01989

Gelfenbaum, G., & Stumpf, R. P. (1993). Observations of currents and density structure across a buoyant plume front. *Estuaries*, *16*(1), 40–52. https://doi.org/10.2307/1352762

Haidvogel, D. B., Arango, H., Budgell, W. P., Cornuelle, B. D., Curchitser, E., Di Lorenzo, E., et al. (2008). Ocean forecasting in terrain-following coordinates: Formulation and skill assessment of the Regional Ocean Modeling System. *Journal of Computational Physics*, *227*(7), 3595–3624. https://doi.org/10.1016/j.jcp.2007.06.016

Halverson, M., & Pawlowicz, R. (2016). Tide, wind, and river forcing of the surface currents in the fraser river plume. *Atmosphere-Ocean*, *54*(2), 131–152. https://doi.org/10.1080/07055900.2016.1138927

Hessner, K., Rubino, A., Brandt, P., & Alpers, W. (2001). The Rhine outflow plume studied by the analysis of synthetic aperture radar data and numerical simulations. *Journal of Physical Oceanography*, *31*(10), 3030–3044. https://doi.org/10.1175/1520-0485(2001)031<3030:TROPSB>2.0.CO;2

Hetland, R. D. (2005). Relating river plume structure to vertical mixing. *Journal of Physical Oceanography*, *35*(9), 1667–1688. https://doi.org/10.1175/jpo2774.1

Hetland, R. D., & MacDonald, D. G. (2008). Spreading in the near-field Merrimack River plume. *Ocean Modelling*, *21*(1–2), 12–21. https://doi.org/10.1016/j.ocemod.2007.11.001

Hickey, B. M., Pietrafesa, L. J., Jay, D. A., & Boicourt, W. C. (1998). The Columbia River Plume Study: Subtidal variability in the velocity and salinity fields. *Journal of Geophysical Research*, *103*(C5), 10339–10368. https://doi.org/10.1029/97JC03290

Honegger, D. A., Ralston, D. K., Jurisa, J., Geyer, R., & Haller, M. C. (2024). Kinematics of an ebb plume front in a tidal crossflow. *Journal of Geophysical Research: Oceans*, *129*(6), e2023JC020550. https://doi.org/10.1029/2023JC020550

Horner-Devine, A. R., Fong, D. A., & Monismith, S. G. (2008). Evidence for the inherent unsteadiness of a river plume: Satellite observations of the Niagara River discharge. *Limnology and Oceanography*, *53*(6), 2731–2737. https://doi.org/10.4319/lo.2008.53.6.2731

Horner-Devine, A. R., Hetland, R. D., & MacDonald, D. G. (2015). Mixing and transport in coastal river plumes. *Annual Review of Fluid Mechanics*, *47*(1), 569–594. https://doi.org/10.1146/annurev-fluid-010313-141408

Horner-Devine, A. R., Jay, D. A., Orton, P. M., & Spahn, E. Y. (2009). A conceptual model of the strongly tidal Columbia River plume. *Journal of Marine Systems*, *78*(3), 460–475. https://doi.org/10.1016/j.jmarsys.2008.11.025

Huguenard, K. D., Bogucki, D. J., Ortiz-Suslow, D. G., & MacMahan, J. H. (2020). Nearshore response to cold air outbreaks in the Gulf of Mexico. *Estuarine, Coastal and Shelf Science*, *235*, 106604. https://doi.org/10.1016/j.ecss.2020.106604

Jay, D. A., Pan, J., Orton, P. M., & Horner-Devine, A. R. (2009). Asymmetry of Columbia River tidal plume fronts. *Journal of Marine Systems*, *78*(3), 442–459. https://doi.org/10.1016/j.jmarsys.2008.11.015

Jurisa, J. T., Nash, J. D., Moum, J. N., & Kilcher, L. F. (2016). Controls on turbulent mixing in a strongly stratified and sheared tidal river plume. *Journal of Physical Oceanography*, *46*(8), 2373–2388. https://doi.org/10.1175/jpo-d-15-0156.1

Kakoulaki, G., MacDonald, D., & Horner-Devine, A. R. (2014). The role of wind in the near field and midfield of a river plume. *Geophysical Research Letters*, *41*(14), 5132–5138. https://doi.org/10.1002/2014GL060606

Kastner, S. E., Horner-Devine, A. R., & Thomson, J. (2018). The influence of wind and waves on spreading and mixing in the Fraser River plume. *Journal of Geophysical Research: Oceans*, *123*(9), 6818–6840. https://doi.org/10.1029/2018JC013765

Kim, C.-K., & Park, K. (2012). A modeling study of water and salt exchange for a micro-tidal, stratified northern Gulf of Mexico estuary. *Journal of Marine Systems*, *96*–*97*, 103–115. https://doi.org/10.1016/j.jmarsys.2012.02.008

Lentz, S. (2004). The response of buoyant coastal plumes to upwelling-favorable winds. *Journal of Physical Oceanography*, *34*(11), 2458–2469. https://doi.org/10.1175/JPO2647.1

Li, C., Li, X., Zhang, G., Boswell, K. M., Kimball, M. E., Shen, D., & Lin, J. (2017). Estuarine plume: A case study by satellite SAR observations and in situ measurements. *IEEE Transactions on Geoscience and Remote Sensing*, *55*(4), 2276–2287. https://doi.org/10.1109/TGRS.2016.2641161

Milliman, J. D., & Farnsworth, K. L. (2013). *River discharge to the coastal ocean: A global synthesis*. Cambridge University Press.

Morey, S. L., Martin, P. J., O'Brien, J. J., Wallcraft, A. A., & Zavala-Hidalgo, J. (2003). Export pathways for river discharged fresh water in the northern Gulf of Mexico. *Journal of Geophysical Research*, *108*(C10), 3303. https://doi.org/10.1029/2002JC001674

Morton, R. A. (2008). Historical changes in the Mississippi-Alabama barrier-island chain and the roles of extreme storms, sea level, and human activities. *Journal of Coastal Research*, *24*, 1587–1600. https://doi.org/10.2112/07-0953.1

Noble, M. A., Schroeder, W. W., Wiseman, W. J., Jr., Ryan, H. F., & Gelfenbaum, G. (1996). Subtidal circulation patterns in a shallow, highly stratified estuary: Mobile Bay, Alabama. *Journal of Geophysical Research*, *101*(C11), 25689–25703. https://doi.org/10.1029/96JC02506

Piñones, A., Valle-Levinson, A., Narváez, D. A., Vargas, C. A., Navarrete, S. A., Yuras, G., & Castilla, J. C. (2005). Wind-induced diurnal variability in river plume motion. *Estuarine, Coastal and Shelf Science*, *65*(3), 513–525. https://doi.org/10.1016/j.ecss.2005.06.016

Ralston, D. K. (2024). Data in support of manuscript "Interacting influences of tides, wind, and river discharge on the outflow plume of Mobile Bay" [Dataset]. *Zenodo*. https://doi.org/10.5281/zenodo.10659126

Ralston, D. K., Geyer, W. R., & Wackerman, C. (2024). Mobile Bay 2021 synthetic aperture radar images [Dataset]. *Woods Hole Open Access Server*. https://doi.org/10.26025/1912/67567

Rijnsburger, S., Flores, R. P., Pietrzak, J. D., Horner-Devine, A. R., & Souza, A. J. (2018). The influence of tide and wind on the propagation of fronts in a shallow river plume. *Journal of Geophysical Research: Oceans*, *123*(8), 5426–5442. https://doi.org/10.1029/2017JC013422

Roth, M. K., MacMahan, J., Reniers, A., Özgökmen, T. M., Woodall, K., & Haus, B. (2017). Observations of inner shelf cross-shore surface material transport adjacent to a coastal inlet in the northern Gulf of Mexico. *Continental Shelf Research*, *137*, 142–153. https://doi.org/10.1016/j.csr.2016.12.017

Schroeder, W. W. (1978). Riverine influence on estuaries: A case study. In *Estuarine interactions* (pp. 347–364). Elsevier.

Schroeder, W. W., Dinnel, S. P., & Wiseman, W. J. (1990). Salinity stratification in a river-dominated estuary. *Estuaries*, *13*(2), 145–154. https://doi.org/10.2307/1351583

Schroeder, W. W., & Wiseman, W. J. (1985). An analysis of the winds (1974–1984) and sea level elevations (1973–1983) in coastal Alabama.

Seim, H. E., Kjerfve, B., & Sneed, J. E. (1987). Tides of Mississippi Sound and the adjacent continental shelf. *Estuarine, Coastal and Shelf Science*, *25*(2), 143–156. https://doi.org/10.1016/0272-7714(87)90118-1

Shchepetkin, A. F., & McWilliams, J. C. (2005). The regional oceanic modeling system (ROMS): A split-explicit, free-surface, topography-following-coordinate oceanic model. *Ocean Modelling*, *9*(4), 347–404. https://doi.org/10.1016/j.ocemod.2004.08.002

Spicer, P., Cole, K. L., Huguenard, K., MacDonald, D. G., & Whitney, M. M. (2022). Wind effects on near- and midfield mixing in tidally pulsed river plumes. *Journal of Geophysical Research: Oceans*, *127*(5), e2022JC018462. https://doi.org/10.1029/2022JC018462

Stumpf, R. P., Gelfenbaum, G., & Pennock, J. R. (1993). Wind and tidal forcing of a buoyant plume, Mobile Bay, Alabama. *Continental Shelf Research*, *13*(11), 1281–1301. https://doi.org/10.1016/0278-4343(93)90053-Z

Thomas, A. C., & Weatherbee, R. A. (2006). Satellite-measured temporal variability of the Columbia River plume. *Remote Sensing of Environment*, *100*(2), 167–178. https://doi.org/10.1016/j.rse.2005.10.018

Wackerman, C. (2023). *Estimating surface currents across fronts using synthetic aperture radar*. NRL/7350/MR—2023/1. U.S. Naval Research Laboratory.

Warrick, J. A., DiGiacomo, P. M., Weisberg, S. B., Nezlin, N. P., Mengel, M., Jones, B. H., et al. (2007). River plume patterns and dynamics within the Southern California Bight. *Continental Shelf Research*, *27*(19), 2427–2448. https://doi.org/10.1016/j.csr.2007.06.015

Whitney, M. M., & Garvine, R. W. (2005). Wind influence on a coastal buoyant outflow. *Journal of Geophysical Research*, *110*(C3), C03014. https://doi.org/10.1029/2003JC002261

Wright, L. D., & Coleman, J. M. (1971). Effluent expansion and interfacial mixing in the presence of a salt wedge, Mississippi River delta. *Journal of Geophysical Research*, *76*(36), 8649–8661. https://doi.org/10.1029/jc076i036p08649

Xia, M., Xie, L., Pietrafesa, L. J., & Whitney, M. M. (2011). The ideal response of a Gulf of Mexico estuary plume to wind forcing: Its connection with salt flux and a Lagrangian view. *Journal of Geophysical Research*, *116*(C8), C08035. https://doi.org/10.1029/2010jc006689

Yuan, Y., Horner-Devine, A. R., Avener, M., & Bevan, S. (2018). The role of periodically varying discharge on river plume structure and transport. *Continental Shelf Research*, *158*, 15–25. https://doi.org/10.1016/j.csr.2018.02.009